On the variability of total electron content over Europe during the 2009 and 2019 Northern Hemisphere SSWs

T. A. Siddiqui[1], Y. Yamazaki [2], C. Stolle [2,3], A. Maute[4], J. Laštovička[5], I. K. Edemskiy[5], Z. Mošna[5]

[1]Leibniz-Institute of Atmospheric Physics at the , Kühlungsborn, Germany
[2] GFZ German Research Centre for Geosciences, Potsdam, Germany
[3]Faculty of Science, University of Potsdam, Potsdam, Germany
[4]High Altitude Observatory, National Center for Atmospheric Research, Boulder, Colorado, USA
[5]Institute of Atmospheric Physics, Czech Academy of Sciences,, Prague, Czech Republic

Key Points:

- The large-scale dynamical variabilities associated with 2009 and 2019 SSWs were simulated using WACCM-X
- Numerical experiments are carried out with TIE-GCM driven by WACCM-X to isolate out the geomagnetic and lower atmospheric effects during both SSWs
- Simulation results show that the TEC variability over Europe was caused predominantly by geomagnetic forcing for the 2019 SSW

Corresponding author: T. A. Siddiqui, siddiqui@iap-kborn.de

Abstract

The nature of the variability of the Total Electron Content (TEC) over Europe is investigated during the 2009 and 2019 Northern Hemisphere (NH) SSW events in this study. As the TEC variability is driven by geomagnetic and lower atmospheric forcing mechanisms, we investigate the dominant drivers and their respective contributions to TEC changes during both SSW events. We simulate the SSWs using the Whole Atmosphere Community Climate Model eXtended version (WACCM-X) and compare the semidiurnal solar and lunar tidal variabilities in the mesosphere-lower thermosphere (MLT) region. Further, in order to assess the mechanisms responsible for the TEC variability during both SSWs, we run numerical experiments using the National Center for Atmospheric Research (NCAR) Thermosphere-Ionosphere Electrodynamics General Circulation Model (TIE-GCM). We constrain the TIE-GCM lower boundary with the WACCM-X fields and carry out simulations both with and without geomagnetic forcing for each of the SSWs. The TIE-GCM simulations allow us to isolate the geomagnetic and lower atmospheric forcing effects on the TEC. We find that there was a major enhancement in daytime TEC over Europe during the 2019 SSW event, which was predominantly geomagnetically forced ($\sim$80%), while for the 2009 SSW, the major variability in TEC was accounted for by lower atmospheric forcing.

1 Introduction

The axial tilt of the Earth creates a strong temperature gradient between the pole and mid-latitudes due to lack of solar heating over the polar regions in wintertime. This temperature gradient along with the Earth's coriolis force results in the formation of stratospheric polar vortex (SPV) that appear over high-latitudes every winter before breaking down in the summer when the polar regions start becoming warmer (e.g., Polvani et al., 2013). The SPV manifests itself in the form of planetary-scale westerly (flowing from west to east) winds that encircle the pole at mid-to higher latitudes. Due to interaction with the planetary waves (PWs) that originate from the troposphere, the SPV experiences large intra- and inter annual variability. The PWs can propagate vertically into the stratosphere when the stratospheric winds are westerly (Charney & Drazin, 1961) and as the PWs break in the stratosphere (McIntyre & Palmer, 1983), they deposit their momentum, which leads to the deceleration of the polar vortex. Due to larger topographic and land-sea contrasts, the PW activity is higher in the Northern Hemisphere (NH) as

compared to the Southern Hemisphere (SH) (e.g., van Loon et al., 1973), which results in the NH stratospheric polar vortex being weaker and much more variable than the one in SH (Waugh & Randel, 1999). Certain extreme cases of PW activity can lead to a breakdown of the polar vortex and a reversal of the westerly flow resulting in magnificent transient meteorological events known as sudden stratospheric warmings (SSWs) (e.g., Scherhag, 1952; Matsuno, 1971).

SSWs are large-scale events that result in an increase in the stratospheric polar temperature usually by several tens of degrees within a few days, which reverses the meridional temperature gradient (i.e., polar temperatures exceed those at mid-latitudes), and concurrently, a deceleration of the westerly zonal mean zonal wind (ZMZW) (e.g., Andrews et al., 1987). In the literature, SSWs are classified as major and minor warmings depending on the extent of increase in polar stratospheric temperature and ZMZW reversal. According to the definition of World Meteorological Organization (WMO), an SSW event is said to be "major" if the westerly zonal mean flow, poleward of 60° at 10 hPa, reverses to easterly along with the reversal of the meridional temperature gradient. A "minor" SSW event occurs when the polar stratospheric temperature increases by at least 25 K within a week or faster. Major SSWs are common in the NH and occur with a frequency of 0.6/year (e.g., Charlton & Polvani, 2007; Butler et al., 2015) whereas SSWs in SH are extremely rare. Along with minor SSWs in August 2010 (Eswaraiah et al., 2017) and September 2019 (Yamazaki et al., 2020), only one major warming in September 2002 (e.g. Baldwin, 2003; Allen et al., 2003) has ever been recorded in the SH.

The breaking of PWs during the SSWs and its associated effects are not only limited to polar stratosphere, but are rather witnessed across different latitudes and altitudes (Pedatella et al., 2018). A mean meridional circulation is induced in the stratosphere as a result of PWs breaking (Haynes et al., 1991), which leads to an upwelling at equatorial latitudes and results in adiabatic cooling over these regions (Fritz & Soules, 1970). Accompanying the warming in the stratosphere is the cooling in the mesosphere at polar latitudes (e.g., Labitzke, 1972; Liu & Roble, 2002) and warming in the mesosphere at equatorial latitudes (e.g., Garcia, 1987; Chandran & Collins, 2014). The NH SSW related effects are also witnessed in the SH in the form of mesospheric warming and a decrease in the occurrence of polar mesospheric clouds through inter-hemispheric coupling mechanisms (e.g., Karlsson et al., 2009; Körnich & Becker, 2010). The associated

effects of NH SSW in the thermosphere have also been reported to result in warming at mid- and high latitudes (e.g., Goncharenko & Zhang, 2008; Funke et al., 2010).

In the last decade, evidence of the SSW impact in the ionosphere, mostly facilitated by the extremely quiet solar and geomagnetic activity levels in the last solar cycle, have been reported in numerous studies following the seminal works by Goncharenko and Zhang (2008) and Chau et al. (2009). Observations have revealed a consistent enhanced semidiurnal perturbation pattern at low-latitudes in ionospheric vertical plasma drifts (e.g., Chau et al., 2009), electron densities (e.g., Lin et al., 2013) and equatorial electrojet (e.g., Vineeth et al., 2009; Fejer et al., 2010; Yamazaki et al., 2012) in response to SSWs. These perturbations have been linked to the changes in migrating semidiurnal solar (SW2) and lunar (M2) atmospheric tides during SSWs. The SW2 and M2 tides are generated in the lower atmospheric regions and are able to propagate upward to the dynamo-region heights where they influence the generation of electric fields in the ionosphere (Baker et al., 1953). The SW2 enhancement during SSWs is thought to be due to the changes in tidal propagation conditions (Jin et al., 2012), non-linear interaction with the stationary PWs (Liu et al., 2010) and changes in the stratospheric ozone distribution (Goncharenko et al., 2012; Siddiqui et al., 2019). The cause of M2 amplification is suggested to be a result of background zonal mean zonal wind changes, which shifts the secondary (Pekeris) resonance peak of the atmosphere towards the period of M2 tide (Forbes & Zhang, 2012). It has also been found during SSWs that the relative enhancement of M2 tide in the mesosphere-lower thermosphere (MLT) and ionosphere is larger than that of SW2 (Pedatella, Liu, Richmond, Maute, & Fang, 2012) and the comparably smaller amplitudes of M2 can even exceed those of SW2 (e.g., Chau et al., 2015; Siddiqui et al., 2018).

A large number of studies that have reported the impact of SSWs on the ionosphere have focused on the variability at low-latitudes (e.g., Chau et al., 2012; Yiğit & Medvedev, 2015, and references therein). In particular, most of these studies have focused on the January 2009 major NH SSW (e.g., Manney et al., 2009), which occurred in the beginning of solar cycle 24 under extremely quiet solar and geomagnetic conditions, and discussed the ionospheric impacts over different longitudinal sectors (e.g., Chau et al., 2010; Goncharenko et al., 2010; Fejer et al., 2010; Xiong et al., 2013; Patra et al., 2014; Yadav et al., 2017; Liu et al., 2019) during this prolonged SSW event. Towards the end of solar cycle 24, another major SSW event was recorded in the NH under similar quiet solar and geomagnetic activity conditions in the final weeks of December 2018 and in the

beginning of January 2019. As the occurrence of SSWs under such favorable conditions is seldom, this event provides us further opportunities to investigate the ionospheric impacts of SSWs. Compared to the investigation of SSW related ionospheric variabilities at equatorial and low-latitudes, the mid-latitude ionosphere variability has not yet been thoroughly investigated. Although the evidence of mid-latitude ionosphere variability during SSWs have been reported in some studies (e.g., Goncharenko et al., 2013; Polyakova et al., 2014; Chen et al., 2016), the Total Electron Content (TEC) data over the European region, which hosts a dense global navigation satellite system (GNSS) networks, have not been much exploited. In this study, we compare the observed TEC over Europe during the 2018/2019 and 2008/2009 SSWs and investigate the dominant mechanisms behind the variabilities using simulations.

The structure of this paper is as follows. In Section 2, the descriptions of the models and the experiments are provided followed by the information about the data sets that are used in this study. In Section 4, we present our results followed by discussion in Section 5. The summary and conclusions from this work are presented at the end.

2 Model descriptions and experiment settings

2.1 WACCM-X

We use WACCM-X version 2.0 (Liu et al., 2018), a configuration of the NCAR Community Earth System Model (CESM 2.0; Hurrell et al., 2013) to perform the model simulations in this study. WACCM-X extends from the surface to the upper thermosphere with its top boundary, depending on the solar and geomagnetic activity, lying between 500 and 700 km. The vertical resolution of WACCM-X above the stratosphere is one fourth of a scale height, and the horizontal resolution is 1.9° x 2.5° in latitude and longitude, respectively. WACCM-X is built upon the Whole Atmosphere Community Climate Model (WACCM) (Marsh et al., 2013) and Community Atmosphere Model version 4 (Neale et al., 2013). The new version of WACCM-X has a coupled ionosphere and incorporates self-consistent low-mid-latitude ionospheric electrodynamics adapted from the Thermosphere-Ionosphere Electrodynamics General Circulation Model (TIE-GCM). At high-latitudes, WACCM-X uses an empirical electric potential pattern (Heelis et al., 1982), which is parameterized by the 3-hour geomagnetic Kp index and an auroral precipitation oval based

on the formulation described by Roble and Ridley (1987). More details about the physical processes included in WACCM-X 2.0 can be found in Liu et al. (2018).

WACCM-X provides a comprehensive tool to study the entire atmosphere-ionosphere system. The impact of lower atmospheric forcing on the upper atmospheric variability can be studied using WACCM-X during specific time periods by constraining the tropospheric and stratospheric dynamics to meteorological reanalysis fields. In the present study, we use the specified dynamics (SD) set up in WACCM-X to simulate the SSWs by constraining the winds and temperatures from 0-50 km towards the National Aeronautics and Space Administration Modern Era Retrospective Analysis for Research and Applications (MERRA) Version 2 (Gelaro et al., 2017). Using the approach described in Kunz et al. (2011), the WACCM-X model fields are constrained to the MERRA2 meteorological fields at every model time step (i.e., 5 min). The default SD-WACCM-X set up does not include forcing from the M2 tide but we implement it in our simulations based on the method described by Pedatella et al. (2012) because the M2 forcing becomes an important source of MLT and ionospheric variability during SSWs. Hourly outputs of winds, temperature and geopotential height are obtained for the 2009 and 2019 SSWs through the SD-WACCM-X runs in this study.

2.2 TIE-GCM

TIE-GCM is a three dimensional, self-consistent numerical model of the coupled thermosphere-ionosphere system that has been developed at the High Altitude Observatory at the National Center for Atmospheric Research (NCAR). The model spans from $\sim$97 km to about 450-600 km depending on the solar cycle activity. In this study, we use TIE-GCM version 2.0 with a horizontal resolution of 2.5° by 2.5° in geographic longitude and latitude and a vertical resolution of 0.25 times the scale height. The input parameters for TIE-GCM include the solar XUV, EUV and FUV spectral fluxes that are defined by the EUVAC model (Richards et al., 1994) using the F10.7 index. The global electric potential due to the wind dynamo is solved by the self-consistent TIE-GCM ionospheric electrodynamo at low- and mid-latitudes. At high-latitudes, however, the electric potential is prescribed through empirical convection electric field patterns using the Heelis (Heelis et al., 1982) or Weimer (Weimer, 2005) models. TIE-GCM also uses an analytical auroral model to account for high-latitude auroral particle precipitation in the

default set up. The upper part of WACCM-X is based on TIE-GCM and it uses this same auroral model.

The effect of lower atmospheric tidal forcing can be specified in TIE-GCM using the tidal perturbations at its lower boundary. The amplitudes and phases of upward propagating atmospheric tides specified at the model lower boundary in the default setup are based on the Global Scale Wave Model (GSWM) (Hagan et al., 1999). The default TIE-GCM lower boundary (LB) assumes constant neutral temperature (T=181 K), geopotential height (Z=96.37 km) and zero horizontal winds (e.g., Maute, 2017). For a more realistic LB conditions, TIE-GCM includes the option to specify hourly inputs at its LB from any other source. In this study, we specify the hourly WACCM-X outputs for the 2009 and 2019 SSWs at the TIE-GCM LB and carry out two simulations for each of the SSWs in order to examine the effects of lower atmospheric forcing on the thermosphere-ionosphere system. In the first simulation setup (hereafter referred to as S1), the TIE-GCM forced by WACCM-X is run in its default setting and the obtained day-to-day ionospheric variability from this run includes the effects of both geomagnetic and lower atmospheric forcings. In the second simulation setup (hereafter referred to as S2), we turn-off the geomagnetic forcing and carry out a similar run for both the SSWs. The day-to-day ionospheric variability resulting from the second run arises solely from lower atmospheric forcing during both SSWs. The geomagnetic forcing is turned off from the TIE-GCM runs by reducing the hemispheric power from 18 GW in the first setup to 0.1 GW and the cross-polar cap potential from 30 kV in the first setup to 0.1 kV. Additionally, the Heelis convection model and the analytical auroral model have also been turned off in the second setup to remove the magnetospheric energy input. The experiment setups used in this study have been summarized in Table 1. We used TIE-GCM instead of WACCM-X to carry out these two simulations because of the former being computationally less expensive than the latter.

3 Data Sets

For this study we use the GPS TEC data from the MIT Haystack Observatory's Madrigal database (Rideout & Coster, 2006), which incorporates the data from over 2000 GPS receivers worldwide. The processed TEC data from the MIT Automated Processing of GPS (MAPGPS) software provides estimates of TEC over 1° by 1° (latitude by

longitude) bins with a temporal resolution of 5 minutes. The unit of GPS TEC data is TECu, where 1 TECu is defined as 10^{16} electrons/m^2.

Hourly values of solar flux ($F_{10.7}$) (Tapping, 2013) have been downloaded from the Space Physics Data facility of the Goddard Space Flight Center through the OMNIWeb data interface to plot the levels of solar activity during the 2009 and 2019 SSWs. The 3-hourly Kp indices are downloaded from the website of German Research Centre for Geosciences (GFZ), Potsdam to monitor the geomagnetic activity levels during the two SSW events. We also use the version 5 temperature data from the Microwave Limb Sounder (MLS) onboard the NASA's Earth Observing System (EOS) Aura satellite (Waters et al., 2006) to compare and validate the temperature obtained from WACCM-X simulations.

4 Results

4.1 Zonal mean and PW variability during 2009 and 2019 SSWs

In Figure 1, the zonal mean temperatures averaged between 70° and 80° N during January - February 2009 (Figures 1a and 1c) and December 2018 - January 2019 (Figures 1b and 1d) from Aura Microwave Limb Sounder (MLS) observations (top panels) and SD-WACCM-X simulations (bottom panels) are presented. The vertical white lines in the figure mark the day of polar vortex weakening (PVW). As an alternative to the classical definition of SSW provided by the WMO, PVW has been used to correlate the tidal enhancements in the MLT and ionosphere with the magnitude of the reversal of stratospheric zonal mean zonal wind (ZMZW) (e.g., Zhang & Forbes, 2014; Chau et al., 2015; Siddiqui et al., 2015). A PVW day is identified by locating the earliest and most extreme reversal of ZMZW at 70°N and 48 km altitude (1 hPa) that occurs simultaneously with the increase in zonal mean temperature at North Pole and 40 km altitude (3 hPa) between December and February.

It can be seen that there is a reasonable agreement between the observed and simulated zonal mean temperatures during the considered time intervals. With the onset of the SSW, the warm stratopause in each of the SSW events starts to descend from its climatological position near 60 km (0.2 hPa) toward lower altitudes resulting in warming at these heights (e.g., Labitzke, 1981) before breaking down completely. The stratopause then reappears at higher altitude before slowly returning to its original location. This

altitudinal shift and reemergence of the stratopause is called an elevated stratopause event and is associated with major SSW events (e.g., Siskind et al., 2007; Manney et al., 2008). In WACCM-X simulations the elevated stratopause events are being reproduced for both the SSWs but their appearances tend to occur slightly earlier in comparison with the Aura MLS observations. The PVW date for the 2009 SSW event occurs on day 2 (Jan 23) and for the 2019 SSW event on day -3 (28 Dec). The warming of the stratosphere is accompanied by cooling in the mesosphere in both these events. In case of 2009 SSW, mesospheric cooling can be observed to start around day 20 above 0.1 hPa in Figure 1a and in the case of 2019 SSW close to day -8 in Figure 1b. The model simulations are able to reproduce these features to a large extent and the overall qualitative agreement in temperature is good but some discrepancies can also be seen especially at altitudes where SD-WACCM-X stops being constrained to MERRA2, i.e. above 50 km ($\sim$1 hPa). The quantitative differences between SD-WACCM-X and Aura MLS observations start to become more clear above this altitude and is more pronounced in the MLT region. These temperature differences could be related to gravity wave forcing, which is parameterized in SD-WACCM-X and may be contributing to the discrepancy between the observations and model simulations (e.g., Smith, 2012).

The left panels of Figure 2 presents the ZMZW at 60°N from SD-WACCM-X for the time intervals that include the 2009 and 2019 SSW events while the right panels show the Kp index and daily solar flux (s.f.u) conditions. The dotted black lines show the PVW days in all the panels. For the 2009 SSW, the ZMZW in the stratosphere between 1-10 hPa changes from eastward to westward direction starting around day 20 in Figure 2a. At 10 hPa, the ZMZW remains in the reversed direction until day 54 while at 1 hPa, where the PVW is defined, the ZMZW reaches a peak reversal on day 23 with a value of about -52 m/s. For the 2019 SSW, the reversal of the ZMZW between 1-10 hPa is seen towards the end of December around day -8 in Figure 2c. The westward direction of ZMZW at 10 hPa remains till day 21 while at 1 hPa, the ZMZW is found to reach a peak reversal on day -3 with a value of -15 m/s. From the comparison of the ZMZW in Figures 2a and 2c, it can be clearly seen that the 2009 SSW event was stronger in terms of ZMZW reversal and more prolonged than the 2019 SSW event.

From the Kp indices and solar flux values in Figures 2b and 2d, it can be inferred that both the 2009 and 2019 SSWs were recorded under periods of low solar and geomagnetic activities. The solar flux levels during the 2009 SSW and 2019 SSWs remained

below 75 s.f.u for both the events. The geomagnetic activity during the onset and peak phase of 2009 SSW hovered mostly around Kp$\leq$ 2+ with an exception on day 19 when Kp values reached 4**o** during the 3-hourly intervals. The 2019 SSW event showed higher geomagnetic activity levels as compared to the 2009 SSW event with brief periods of spike in Kp values that reached up to 4+ on day -3 (Dec 28) and 5**o** on day 5 but overall the period during the 2019 SSW remained geomagnetically quiet.

Figure 3 presents the variability of PWs with wave number 1 (PW1) and 2 (PW2) at 10 hPa in temperature from SD-WACCM-X for the 2009 and 2019 SSWs. In this figure, the colorbar scales of PW1 are chosen to be twice as large in magnitude as compared to those for PW2. In Figures 3a and 3c, the amplitudes of PW1 and PW2, respectively, are presented for the 2009 SSW event. The enhancement of PW1 is seen in NH high-latitudes particularly around 60°N with peaks on days 6 and 22 while in case of PW2, the enhancement begins in the second week of January and peaks on day 19. Based on the enhanced amplitudes of PW2 in Figure 3c, we find that our results are consistent with earlier studies (e.g., Manney et al., 2009) that have classified the 2009 SSW as PW2 forced split SSW event. The amplitudes of PW1 and PW2 for the 2009 SSW are also similar to the results shown by Pedatella et al. (2014) using four different whole atmosphere models.

The amplitude of PW1 and PW2 in temperature are presented in Figures 3b and 3d, respectively, for the 2019 SSW event. The PW1 amplitudes show enhancement poleward of 60°N during December with maxima on day -7. The peak PW1 amplitudes for this event are almost twice as large as compared to that of peak PW1 for the 2009 SSW. The PW2 amplitudes are smaller in magnitude as compared to that of PW1 for this event but enhancement in PW2 is also seen poleward of 60°N towards the end of December with maxima centered on day -9. The 2019 SSW has been classified in literature as neither a typical displaced nor a typical split SSW event (Rao et al., 2019) but rather a mixed type event, which was initially a displaced SSW and later became a split SSW. From Figure 3b, it can be inferred by the dominance of PW1 amplitudes that the 2019 SSW must have started as a displaced SSW event.

4.2 Migrating semidiurnal tides during 2009 and 2019 SSWs

It is well established now that the primary reason for the variability in the MLT and ionosphere during SSWs is due to the modulation of atmospheric tides. In particular, the variability of SW2 and M2 have been found to be the most significant based on modeling and observational studies (e.g., Vineeth et al., 2009; Chau et al., 2009; Fejer et al., 2010; Pedatella & Forbes, 2010; Goncharenko et al., 2012; Yamazaki et al., 2012; Forbes & Zhang, 2012; Lin et al., 2013; Pedatella et al., 2014; He et al., 2017; Siddiqui et al., 2018; Hibbins et al., 2019). Atmospheric tides refer to planetary-scale oscillations of the atmosphere that are mainly excited by gravitational forces of the moon and by thermal forcing from the sun (e.g., Lindzen & Chapman, 1969; Forbes & Garrett, 1978; Forbes, 1982). These oscillations have periods and sub-periods of a solar or a lunar day. The solar tides form the dominating component of the tidal oscillations and are predominantly thermally forced. The excitation mechanisms include daily periodic absorption of solar energy by tropospheric water vapour and stratospheric ozone (e.g., Forbes & Wu, 2006; Zhang et al., 2010) while the relatively smaller lunar tides are mainly forced due the lunar gravitational effects on the Earth's atmosphere. In this section, we investigate the variability of the migrating semidiurnal solar (SW2) and semidiurnal lunar (M2) tides during the two SSW events.

The hourly outputs of neutral temperature from SD-WACCM-X simulations are used to extract the components of the solar and lunar tides by performing a least squares fit with a moving window of 15 days at each latitude. The following equation based on Pedatella et al. (2012) has been used to make the fit:

$$\sum_{n=0}^{3}\sum_{s=n-5}^{n+5} A_{n,s}\cos(n\Omega t + s\lambda - \phi_{n,s}) + \sum_{s=-3}^{3} L_s cos(2\tau + (s-2)\lambda - \Phi_{n,s}) \quad (1)$$

where $\Omega = \frac{2\pi}{24}$ hour^{-1}, t is universal time in hours, n denotes the harmonics of a solar day, λ is the longitude, s is the zonal wave number, $A_{n,s}$ and $\phi_{n,s}$ are the amplitude and phase of the respective solar tidal components. For a wave propagating westward $s > 0$, while for a wave propagating eastward $s < 0$. L_s and $\Phi_{n,s}$ represent the amplitude and the phase of the semidiurnal lunar tide, respectively.

Figure 4 presents the amplitudes and phases of the SW2 (top panels) and M2 (bottom panels) tides in neutral temperature at 1×10^{-4} hPa (∼110 km altitude) from SD-

WACCM-X simulations between January and February 2009. The vertical white lines mark the day of PVW. In Figure 4a, the SW2 tidal variability shows enhanced amplitudes of up to 21 K at Southern Hemisphere (SH) mid-latitudes on day 15 and then again amplitudes of over 25 K around day 35. In the NH, the SW2 enhancements are only seen after day 25 but enhanced amplitudes of up to 24 K are found from simulations. Following the PVW day, there is a sudden decrease in the amplitude of SW2 at SH mid-latitudes. This feature of SW2 was also reported in a study by Pedatella et al. (2014) where they compared the temporal variability of SW2 during the 2009 SSW event using four different whole atmosphere models. Figure 4c presents the amplitude of M2 tide where we notice its enhancement in both hemispheres a few days after the PVW day. Another enhancement of M2 is seen in the NH after day 40. The M2 variability from SD-WACCM-X during this SSW event is consistent with the results of Zhang and Forbes (2014), in which similar observations of M2 have been reported from neutral temperature measurements at 110 km from the Sounding of the Atmosphere using Broadband Emission Radiometry (SABER) instrument onboard the Thermosphere Ionosphere Mesosphere Energetics Dynamics (TIMED) satellite. The SW2 and M2 phases in UT are presented in Figures 4b and 4d, respectively. At NH low- and mid-latitudes, the SW2 phase shows a noticeable change in phase before and after the peak PVW day. At SH mid-latitudes, there is a change in SW2 phase of up to 1 h coinciding with the weakening of SW2. The decrease of SW2 phase by a few hours in the ionosphere was also reported by Pedatella et al. (2014) and Lin et al. (2013) during the period where the SW2 amplitude weakened. The phase of the M2 tide shows more discernible phase shifts at low- and mid-latitudes around the PVW, which becomes relatively more stable after day 40.

Figure 5 shows the amplitudes and phases of SW2 and M2 tides in neutral temperature at 1×10^{-4} hPa ($\sim$110 km altitude) between December 2018 and January 2019. Similar to the SW2 variability during the 2009 SSW event, the SW2 amplitude in Figure 5a shows enhancement at SH mid-latitudes on either side of the PVW day with a reduction of SW2 amplitude in between. The SW2 amplitude reaches a peak of around 17 K on day -12 and around 20 K on day 8 in the SH. In the NH, the SW2 amplification starts close to the PVW day and it reaches a value of around 18 K on day 9. In Figure 5c, the first M2 enhancement in SH with peak amplitudes of around 6.5 K happens a few days after the PVW day. The second M2 enhancement in the SH with peak amplitude of around 7.5 K is seen on day 11. Following Chau et al. (2015) and Conte et al.

(2017), we also performed tidal analyses using a 21-day running window to further reduce any artifacts or ambiguity between the determination of SW2 and M2 tides but we still found the amplification of M2 to be similar to as shown in Figure 5c using a 15-day window. We find that the M2 amplitude during the 2019 SSW is far smaller as compared to that during the 2009 SSW event. One reason for the difference in amplification could be related to the timing of the SSW event relative to the phase of the moon. Pedatella and Liu (2013) have shown from simulation results that the lunar tidal response in the ionosphere is dependent upon the phase of the moon relative to the timing of the SSW event. Further, Fejer et al. (2010) have found that the lunar effects in the ionosphere during SSWs amplify close to the new or the full moon days. The new moon day for the 2009 SSW occurred 3 days after the PVW day while for the 2019 it was recorded 6 days before the PVW. This difference in the timing of the new moon days relative to the PVW days may also be contributing to the reduced amplification of M2 during the 2019 SSW. The SW2 and M2 phases are presented in Figures 5b and 5d, respectively. At low-latitudes in NH, the SW2 phase shows a decrease of 1-2 hours around the PVW day. The decrease in the phase is also seen in the SH around the PVW day similar to the reduction seen during the 2009 SSW event. From the M2 phase plot it is found that the M2 phase shift is more noticeable in the SH as compared to the NH around the PVW day.

Figure 6 presents the M2 tidal amplitudes for the 2009 and 2019 SSW events obtained using the V2.0 temperature measurements from the SABER instrument onboard the TIMED satellite. We employ the least-squares fitting method mentioned in Zhang and Forbes (2014) to determine the M2 amplitudes from zonally averaged SABER temperature residuals. As the period of the M2 tide from the frame of the TIMED satellite is 11.85 days (Forbes et al., 2013), we use a 12-day moving window and fit only the M2 tide to the daily zonally averaged temperature residuals. Figures 6a and 6b show the amplitude of the M2 tide for the 2009 and 2019 SSWs, respectively. The vertical white lines show the days of PVW. The enhancement of M2 following the PVW can be seen at low- and mid- latitudes for the 2009 SSW event in Figure 6b. This plot of M2 amplitude is similar to the one shown in Zhang and Forbes (2014) (see Figure 1). The M2 tides in neutral temperature from SD-WACCM-X simulations for the 2009 SSW, shown in Figure 4c, match very well with the M2 from SABER temperature observations in terms of the timing of the M2 enhancement. In the NH, the variability of the M2 amplitudes from SD-WACCM-X simulations is slightly more consistent with those obtained from

SABER temperature observations as the M2 peaks are located at similar latitudes. In the SH, the M2 peaks from SABER observations on day 27 are slightly more equatorward as compared to those from SD-WACCM-X simulations. The M2 amplitudes for the 2019 SSW presented in Figure 6b shows that the level of M2 enhancement for this SSW was clearly lower than for the 2009 SSW. The M2 enhancements can be seen to occur towards the end of December 2018 between days -7 and 0 poleward of 40°S and around day 22 above 20°N. The enhancement in the SH towards the end of December is also captured in M2 from SD-WACCM-X simulations in Figure 5c. But the M2 amplitudes from SD-WACCM-X do not exactly reproduce the observations for the 2019 SSW event as the M2 peak around day 22 in the NH is not seen in the simulations. There is similarity between the observed and simulated M2 amplitudes in the sense that the enhancements were particularly weaker for the 2019 SSW as compared to the 2009 SSW event, which is confirmed from both the simulated and observed M2 amplitudes.

4.3 GPS TEC variability over Europe during 2009 and 2019 SSWs

In this section of the paper, we first analyze the variability of TEC over Europe from GPS observations during the 2019 SSW. The readers may note that there has been a change in the order of presentation of the SSWs in this section. The GPS TEC observations over Europe during the 2009 SSW is presented later for the purpose of comparison. Following Goncharenko et al. (2010), we first define the mean state of the quiet-time TEC during the 2019 SSW to investigate the TEC variability over Europe associated with this event. We select the quiet period prior to the SSW onset between 11 and 20 December, 2018 with Kp$\leq$ 3 on most days and solar flux levels below 70 s.f.u. to estimate the mean TEC values. The perturbations in TEC during the 2019 SSW, ΔTEC, is then calculated by using,

$$\Delta TEC = TEC - TEC_{mean} \tag{2}$$

In Figure 7, we present the ΔTEC (in TECu) observed between December 26, 2018 and January 6, 2019 at 12 UT over Europe. The most notable feature in this figure is the large positive ΔTEC that is recorded on December 28 over the whole region in general and over the South-West part of Europe in particular. Apart from this day, ΔTEC values also show notable enhancements over Europe the following day on December 29

and again on January 5 but with lower magnitudes. A depletion in ΔTEC across Southern Europe is also observed on January 3. We take the averaged value of TEC over the region shown in Figure 7 for each UT and present the temporal evolution of averaged TEC (Figure 8a) and ΔTEC (Figure 8b) across Europe as a function of local time. We use latitudinal and longitudinal bands between 35°-60°N and 15°W-30°E, respectively, to calculate these values. The dotted black lines mark the PVW day. The diurnal variation of TEC is evident in Figure 8a with the TEC values increasing gradually from morning to afternoon hours and then after attaining a maximum during afternoon decreasing gradually post sunset. The day-to-day variability of TEC, which is subject to solar, geomagnetic and lower atmospheric forcing, can also be seen in Figure 8a. The spike in both averaged TEC and ΔTEC values on days -3 (Dec 28) and -2 (Dec 29) between 10-12 UT is also clear in this figure. From the Kp values shown for this time interval in Figure 2d, we notice that there was an increase in Kp index on December 28 with the maximum values on this day reaching up to 4+ and not decreasing below 3*o*. It is also to be noted that the timing of TEC enhancement is coinciding with the PVW day for the 2019 SSW event. As the influence of SSW events on the variability of TEC is now relatively well known (e.g., Goncharenko et al., 2010; Yue et al., 2010; Sumod et al., 2012; Goncharenko et al., 2013; Polyakova et al., 2014; Vieira et al., 2017), there is a motivation to investigate whether the TEC and ΔTEC spikes were linked to increased atmospheric forcing or to geomagnetic forcing. In the next section, we investigate the dominant forcing mechanism that is causing this TEC variability over Europe in more detail with the help of TIE-GCM simulations but first we present the TEC and ΔTEC variability over Europe for the 2009 SSW event in Figure 9 for comparison with those from the 2019 SSW.

We first select the quiet period prior to the SSW onset between 3 and 12 January, 2009 with Kp$\leq$ 3 on most days and solar flux levels below 70 s.f.u. to estimate the quiet-time mean TEC values. These exact dates have been used by Goncharenko et al. (2010) in an earlier study to characterize the mean behavior of the quiet-time ionosphere during the 2009 SSW. ΔTEC is then calculated using equation 2 as before. Along with the diurnal and day-to-day variability of TEC, we see major TEC enhancements in Figure 9a between 10 and 12 UT on days 41 and 46. In Figure 9b, ΔTEC shows the perturbations of TEC from the quiet-time mean values and the large TEC perturbations particularly after day 40 is more clearly noticeable. The spikes in ΔTEC on days 41 and 46

between 10-12 UT are 3-5 TECu greater than the mean TEC values at these hours. We have limited the presentation of TEC data to day 50 to minimize the effects of seasonal transition as daytime TEC values start to depart from the calculated mean values. We notice from Figure 2c that the Kp values on day 41 remained below 1 and on day 46 below 3. Further, the solar flux values ranged between 65-68 s.f.u. on these days. Based on the levels of geomagnetic activities on these days, it is fair to assume that this TEC driver solely cannot explain the large TEC perturbations that are witnessed in Figure 9b. From the results of Goncharenko et al. (2012), it is known that the TEC variances (computed as a departure from the mean daytime values) at low-latitudes in the American sector can be up to 5 times larger than those obtained from the International Reference Ionosphere (IRI) model for almost a month after the 2009 SSW event. The large TEC variances in their study was attributed to the modified tidal forcing associated with the 2009 SSW. In the next section, we explore using TIE-GCM simulations whether the enhancement in the averaged TEC plot in Figure 9a is also linked to the increased lower atmospheric forcing during the 2009 SSW event.

5 Discussions

5.1 Variability of simulated TEC over Europe during 2009 and 2019 SSWs

Based on the GPS observations, it seems that the TEC variability over Europe during the 2019 SSW may also be affected by moderately enhanced geomagnetic activity levels as seen by the increase in Kp values. As the TEC variability is influenced by both geomagnetic and lower atmospheric forcing, it is imperative to separate the effects of these two processes and assess their individual contributions towards the variability of TEC. To separate the influence of geomagnetic and lower atmospheric forcing on the TEC, we carry out two simulations using TIE-GCM. For the 2019 SSW, the TIE-GCM model is run with and without geomagnetic forcing to isolate the mechanisms behind the TEC variability during these events. In Figure 10, the TEC over Europe, which is derived from TIE-GCM simulations, is presented for the 2019 SSW. Figure 10a shows the average TEC over Europe for the TIE-GCM run where both the geomagnetic and lower atmospheric forcings have been switched on (S1). We note that the TEC derived from TIE-GCM simulations are able to reproduce the TEC spikes on days -3 (Dec 28) and 5 (Jan 5) and are qualitatively similar in comparison to the averaged GPS TEC in Figure 8a. The modeled and observed TEC may only be compared in a qualitative sense owing to the up-

per boundary limit of TIE-GCM, which extends to only about 750 km in altitude, hinders a quantitative comparison with GPS TEC observations. The modeled TEC results demonstrate that the TIE-GCM simulation includes the various forcing mechanisms that are responsible for the observed TEC variability and can be used to filter the TEC variability associated with SSW. The averaged TEC enhancements over Europe reach values of about 8.5 TECu at 12 UT on day -3 and 6.5 TECu at 13 UT on day 5. In comparison to the quiet-time seasonal TEC levels, the TEC spikes represent an increase of more than 100% at 12 UT on day -3 and more than 50% at 13 UT on day 5, which is due to the combined effects of geomagnetic and lower atmospheric forcing.

In Figure 10b, the averaged TEC over Europe is presented for the TIE-GCM run where the geomagnetic forcing have been switched off and only lower atmospheric forcing remains active (S2). It can be noticed that there is an apparent reduction of the averaged TEC values after turning off geomagnetic forcing and the peak TEC values have been reduced to less than 5 TECu. The major TEC enhancements in this plot can be seen on days -3 and 4 with peak TEC values reaching 5 and 4.5 TECu, respectively, between 10-14 UT. In Figure 10c, the difference of TEC values from the two simulations (TEC_{diff}=TEC_{S1}−TEC_{S2}) is presented. The filled contour lines are plotted when absolute value of TEC_{diff} exceeds 1 TECu. It can be clearly noted that the major difference in TEC is seen on days -3 and 5 when TEC_{diff} values between 12-14 UT reach 3.6 and 2.3 TECu, respectively. Through this plot, the contribution to TEC variability solely due to geomagnetic forcing can be assessed. It can also be easily inferred that the major processes behind the averaged TEC spikes on days -3 and 5 between 10-14 UT are related to geomagnetic forcing. For a quantitative breakdown of the contribution of geomagnetic and lower atmospheric forcing to TEC variability, we first calculate the seasonal TEC levels ($\mathrm{TEC}_{seasonal}$) from the quiet-days between 11 and 20 December in TEC_{S2}. The contribution of geomagnetic forcing, in percentage, to the TEC variability can then be calculated by using the relation,

$$\frac{TEC_{diff} \times 100\%}{(TEC_{S1} - TEC_{seasonal})} \tag{3}$$

The contribution of geomagnetic forcing to the TEC variability in percentage is plotted through the dashed black and blue open contour lines at 40 and 80% levels, respectively.

For the TEC enhancements on day -3 (Dec 28) at 12 UT, the geomagnetic contribution comes out to be 78% and the remaining 22% is the contribution due to lower atmospheric forcing. In case of the TEC enhancements on day 5 (Jan 5) at 12 UT, the geomagnetic and lower atmospheric contributions comes out to be about 82% and 18%, respectively.

The individual contributions of the geomagnetic and lower atmospheric forcing on the TEC variability over Europe is also assessed for the 2009 SSW event. We present the averaged TEC over Europe derived from TIE-GCM simulations for the 2009 SSW in Figure 11. The averaged TEC derived from the TIE-GCM run with S1 and S2 setups are presented in Figure 11a and 11b, respectively. A qualitative comparison with the GPS TEC observations in Figure 9a suggests that the primary features of the averaged TEC variability have been consistent in the simulations. The comparatively lower levels of averaged TEC before day 30 between 10-15 UT and the moderately enhanced averaged TEC levels after this day has been correctly reproduced in the simulation. The spike in the average TEC on day 45 (February 14), seen more pronounced in Figure 9a, has also been reproduced in the simulations but it is delayed by an hour in comparison with the observations. The spike in TIE-GCM derived TEC reaches 5.3 TECu on day 45 at 13 UT. Compared to the quiet-time seasonal variations at this UT, which is calculated using the TEC values between day 3 and 12, the increase in TEC comes out to be 1.2 TECu on day 45. This represents an increase in TEC values by about 30% from seasonal variations. In comparison with the 2019 SSW, we notice that the major source of averaged TEC variability for the 2009 SSW comes due to the lower atmospheric forcing. This point becomes even more clear through Figure 11c, which shows the difference of the averaged TEC values from the two simulations. The filled contour lines in this figure are again shown for values greater than 1 TECu and the dashed open contour lines mark the contribution of the geomagnetic forcing to the TEC variability in percentage. We notice that unlike the 2019 SSW, the TEC difference plot for the 2009 SSW points to reduced contribution from geomagnetic forcing to the average TEC variability over Europe during this SSW.

5.2 Possible reasons for the observed TEC variability

Most of the studies that have documented the ionospheric effects of SSWs, especially during the 2009 SSW, have focused on the variability at equatorial and low-latitudes

(e.g., Chau et al., 2012; Yiğit & Medvedev, 2015, and references therein). While it is now accepted that the mechanisms causing the variability at these latitudes are driven by the changes in the vertically propagating semidiurnal solar and lunar tides, the mechanisms responsible for the mid-latitude ionospheric variability during SSWs are not as well understood. Simulation results by Pedatella and Maute (2015) have shown that the variability of the mid-latitude ionospheric F-region peak height (hmF2) during SSWs is predominantly driven by the field-aligned neutral winds, which is modulated by the M2 tidal enhancements. Yue et al. (2010) observed the global ionospheric response using Constellation Observing System for Meteorology, Ionosphere, and Climate (COSMIC) satellites during the 2009 SSW and suggested the changes in the neutral wind and composition due to direct propagation of tides as another mechanism for the ionospheric mid-latitude variability during SSWs. It is also known from observations and modeling studies that the influence of SSWs at mid- and high-latitudes ionosphere is generally smaller as compared to that at low-latitudes. Oyama et al. (2014) used the FORMOSAT-3/ COSMIC peak ionospheric electron density (NmF2) data and found that changes in mid-latitude NmF2 to be only between 20-30% during the 2009 SSW, which was comparably much lower than the changes at low-latitudes. Their observation results were found to be consistent with the simulations shown by Pedatella and Maute (2015). For the 2009 and 2019 SSW event, our results also show similar numbers as the TEC variability over Europe increases by $\sim$20-30% with respect to seasonal variations due to SSW associated effects.

During the 2019 SSW event, along with the increase in Kp values to 4+ on December 28, the meridional component of the interplanetary magnetic field (IMF) in Geocentric Solar Magnetospheric (GSM) coordinate system, B_z turned southward and reached up to -7.5 nT, the Auroral Electrojet (AE) index reached to levels >500 nT. The symmetric disturbance field in H (SYM-H) index declined from 26 nT on December 27 to -30 nT on December 28. Based on the statistical measures, the geomagnetic activity parameters resemble the conditions of a weak geomagnetic storm (e.g., Yokoyama & Kamide, 1997). The sudden surge in TEC observations over Europe on December 28 between 10-12 UT as seen in Figure 7 could be resulting due to a result of the positive storm effect mechanism. During geomagnetic storms, the relative increase in the ionospheric plasma with respect to quiet-time conditions is referred to as positive storm effect or positive ionospheric storms. (e.g., Matsushita, 1959; Goncharenko et al., 2007; Astafyeva et al., 2016). The positive storm effect can arise due to the change in the direction of the merid-

ional thermospheric winds from poleward to equatorward, which results in the transport of plasma along the magnetic field lines to altitudes where the recombination rates are lower (e.g., Jones & Rishbeth, 1971). During daytime, this results in an increase in the F-region plasma densities. Another mechanism that plays an important role in the increase of plasma densities during geomagnetic storms is the penetration of high-latitude convection electric fields into the low-latitude ionosphere. This phenomenon more commonly known as prompt penetration electric fields (PPEF) (e.g., Sastri, 1988; Abdu et al., 1995) can increase the plasma densities in the equatorial ionization anomaly (EIA) and shift the EIA crests poleward, in some cases, by upto 15 degrees in latitude (e.g., Astafyeva et al., 2020). The poleward shift of the EIA may also result in the observed TEC surge over Europe. During geomagnetically active times, ionospheric plasma densities is driven by a combination of these drivers and the interplay of these processes could be responsible for the observed spike in TEC seen across Europe in Figure 7.

It is well known that the dynamics of the thermosphere-ionosphere system is greatly modified due to increased geomagnetic forcing processes at high-latitudes (e.g., Prölss, 1995). Pedatella (2016) performed a numerical simulation using TIE-GCM that showcased the ionospheric variability in response to a SSW event that was contrived to occur simultaneously along with a major geomagnetic storm. The results from their study showed that the TEC changes due to a geomagnetic storm are significantly (∼50-100%) different when the effects of SSW were included in the simulation. Pedatella (2016) concluded that the changes in the thermospheric composition due to SSWs (Korenkov et al., 2012) may influence the geomagnetic storm related composition changes in the thermosphere. The TEC variability over Europe seen in Figure 7 could also be influenced by the changes in thermospheric composition due to both SSW and geomagnetic related effects. However, more research is needed to understand the role and contribution of thermospheric composition changes due to different drivers that lead to ionospheric variabilities.

Similar to the 2019 SSW event, another SSW event in January 2012 was accompanied by a moderate geomagnetic storm and the TEC disturbances during this period were studied at low- and mid-latitudes in the Brazilian sector by Vieira et al. (2017). Similar to our observations in Figure 7, a spike in daytime TEC values, was seen in their results following the occurrence of a moderate geomagnetic storm during this SSW event. To separate the potential contribution of geomagnetic and lower atmospheric drivers that

are responsible for the TEC variability, Vieira et al. (2017) used a regional empirical TEC model. Another study by Liu et al. (2019) analyzed the TEC response to the 2018 SSW at low- and mid-latitude stations in China and attempted to separate the effects of ionospheric drivers on TEC by correlating the TEC perturbations with F10.7 solar flux, Ap index and the solar wind speed. Spikes in TEC on certain days during this event was attributed to the increased geomagnetic activity in their study. The use of simulations to study the ionospheric effects solely due to lower atmospheric forcing have been implemented in some earlier studies. Pedatella and Maute (2015) simulated the ionospheric effects during the 2013 SSW event only due to lower atmospheric forcing by running the TIME-GCM simulations under constant solar and geomagnetic activity levels. Yamazaki et al. (2014) used a similar method by running the TIE-GCM under constant solar and magnetospheric energy inputs to study the day-to-day variability of the equatorial electrojet due to lower atmospheric forcing. Our method builds upon the techniques that are presented in Pedatella and Maute (2015) and Yamazaki et al. (2014) and provides a tool to separate the geomagnetic and lower atmospheric forcing effects on the ionospheric variability. The occurrence of an SSW event during quiet-time ionospheric conditions is a rarity and there have been many SSWs that occur under active geomagnetic conditions, which complicates the separation of SSW driven ionospheric variability.

6 Conclusions

The variability in the mid-latitude TEC over Europe was investigated during the 2019 SSW in the present study using GPS TEC observations and TIE-GCM simulations. The main feature of the TEC response during this SSW was a dramatic spike in the daytime TEC that lasted for a couple of days. The geomagnetic activity indices suggest that the 2019 SSW period was also accompanied by weak geomagnetic storm like conditions, which coincided with the spike in TEC values. As the TEC variability is influenced by both geomagnetic and lower atmospheric forcings, we used TIE-GCM simulations to investigate the contributions of each of the individual mechanisms towards the TEC enhancement. To quantify the isolated influence of either geomagnetic or lower atmospheric forcing on TEC, we first force the TIE-GCM lower boundary with the output from WACCM-X simulations performed over the 2019 SSW period, and then conduct two numerical simulations. The first TIE-GCM simulation includes both geomagnetic and lower atmospheric forcing while in the second simulation the geomagnetic forcing has been turned off. We

ascertain the individual contributions of geomagnetic and lower atmospheric forcing towards the sudden TEC enhancement that is witnessed during the 2019 SSW through these two simulations. We further compare the TEC variability during 2019 SSW over Europe with that of the TEC variability during the 2009 SSW. Based on the results we summarize our findings as follows:

1. It is found that the spike in TEC over Europe during the 2019 SSW is forced dominantly due to increase in geomagnetic activity which accounts for about $\sim$80% of the TEC variability while the remaining variability is accounted for by the lower atmospheric forcing.

2. In contrast, the variability of TEC over Europe during the 2009 SSW event was up to 30% in comparison to seasonal variations and was predominantly due to lower atmospheric forcing.

3. The mid-latitude TEC variability associated with lower atmospheric forcing during the 2019 SSW lies between 20-30% relative to seasonal TEC values, which is similar to the levels reported by previous observation and modeling based studies that documented the mid-latitude ionospheric variability during the 2009 SSW.

Acknowledgments

We thank the Aura/MLS team and NASA/JPL for the microwave limb sounding measurements and the availability of the level2 data set at the Aura Validation Data Center (http://avdc.gsfc.nasa.gov/). The geomagnetic activity index Kp was provided by the GFZ German Research Centre for Geosciences (https://www.gfz-potsdam.de/en/kp-index/). The solar activity index F10.7 was downloaded from the SPDF OMNIWeb database (https://omniweb.gsfc.nasa.gov). The ground-based GPS TEC data are available through the MIT Haystack Observatory Madrigal database (http://madrigal.haystack.mit.edu/madrigal/). The neutral temperature obtained from WACCM-X simulation for the 2009 SSW event have been publicly made available and uploaded through the Mendeley data set with the following link (http://dx.doi.org/10.17632/47pnw8pgmk.1). For the 2019 SSW, it can be found with the following link (http://dx.doi.org/10.17632/48257xrmx3.1). T.A.S acknowledges support from Humboldt research Fellowship for Postdoctoral Researchers. This material is based upon work supported by the National Center for Atmospheric Re-

search, which is a major facility sponsored by the National Science Foundation under Cooperative Agreement No. 1852977. This work was supported in part by the European Space Agency through Contract 4000126709/19/NL/IS "VERA".

References

Abdu, M., Batista, I., Walker, G., Sobral, J., Trivedi, N., & de Paula, E. (1995). Equatorial ionospheric electric fields during magnetospheric disturbances: local time/longitude dependences from recent EITS campaigns. *Journal of Atmospheric and Terrestrial Physics*, *57*(10), 1065 - 1083. doi: https://doi.org/10.1016/0021-9169(94)00123-6

Allen, D. R., Bevilacqua, R. M., Nedoluha, G. E., Randall, C. E., & Manney, G. L. (2003). Unusual stratospheric transport and mixing during the 2002 Antarctic winter. *Geophysical Research Letters*, *30*(12). doi: 10.1029/2003GL017117

Andrews, D. G., Holton, J. R., & Leovy, C. B. (1987). *Middle atmosphere dynamics* (No. 40). Academic press.

Astafyeva, E., Bagiya, M. S., Förster, M., & Nishitani, N. (2020). Unprecedented hemispheric asymmetries during a surprise ionospheric storm: A game of drivers. *Journal of Geophysical Research: Space Physics*, *125*(3), e2019JA027261. doi: 10.1029/2019JA027261

Astafyeva, E., Zakharenkova, I., & Pineau, Y. (2016). Occurrence of the dayside three-peak density structure in the F2 and the topside ionosphere. *Journal of Geophysical Research: Space Physics*, *121*(7), 6936-6949. doi: 10.1002/2016JA022641

Baker, W., Martyn, D. F., et al. (1953). Electric currents in the ionosphere-the conductivity. *Phil. Trans. R. Soc. Lond. A*, *246*(913), 281–294.

Baldwin, M. (2003). Major stratospheric warming in the southern hemisphere in 2002: Dynamical aspects of the ozone hole split. *SPARC newsletter*, *20*, 24–26.

Butler, A. H., Seidel, D. J., Hardiman, S. C., Butchart, N., Birner, T., & Match, A. (2015). Defining sudden stratospheric warmings. *Bulletin of the American Meteorological Society*(2015). doi: 10.1175/BAMS-D-13-00173.1

Chandran, A., & Collins, R. (2014). Stratospheric sudden warming effects on winds and temperature in the middle atmosphere at middle and low latitudes: a

study using WACCM. *Annales Geophysicae (09927689)*, *32*(7).

Charlton, A. J., & Polvani, L. M. (2007). A new look at stratospheric sudden warmings. Part I: Climatology and modeling benchmarks. *Journal of Climate*, *20*(3), 449–469. doi: 10.1175/JCLI3996.1

Charney, J. G., & Drazin, P. G. (1961). Propagation of planetary-scale disturbances from the lower into the upper atmosphere. *Journal of Geophysical Research (1896-1977)*, *66*(1), 83-109. doi: 10.1029/JZ066i001p00083

Chau, J. L., Aponte, N. A., Cabassa, E., Sulzer, M. P., Goncharenko, L. P., & González, S. A. (2010). Quiet time ionospheric variability over Arecibo during sudden stratospheric warming events. *Journal of Geophysical Research: Space Physics*, *115*(A9). (A00G06) doi: 10.1029/2010JA015378

Chau, J. L., Fejer, B. G., & Goncharenko, L. P. (2009). Quiet variability of equatorial ExB drifts during a sudden stratospheric warming event. *Geophysical Research Letters*, *36*(5). doi: 10.1029/2008GL036785

Chau, J. L., Goncharenko, L. P., Fejer, B. G., & Liu, H.-L. (2012, 01). Equatorial and low latitude ionospheric effects during sudden stratospheric warming events. *Space Science Reviews*, *168*(1), 385–417. doi: 10.1007/s11214-011-9797-5

Chau, J. L., Hoffmann, P., Pedatella, N. M., Matthias, V., & Stober, G. (2015). Upper mesospheric lunar tides over middle and high latitudes during sudden stratospheric warming events. *Journal of Geophysical Research: Space Physics*. (2015JA020998) doi: 10.1002/2015JA020998

Chen, G., Wu, C., Zhang, S., Ning, B., Huang, X., Zhong, D., ... Huang, L. (2016). Midlatitude ionospheric responses to the 2013 SSW under high solar activity. *Journal of Geophysical Research: Space Physics*, *121*(1), 790-803. doi: 10.1002/2015JA021980

Conte, J. F., Chau, J. L., Stober, G., Pedatella, N., Maute, A., Hoffmann, P., ... Murphy, D. J. (2017). Climatology of semidiurnal lunar and solar tides at middle and high latitudes: Interhemispheric comparison. *Journal of Geophysical Research: Space Physics*, *122*(7), 7750–7760.

Eswaraiah, S., Kim, Y. H., Liu, H., Ratnam, M. V., & Lee, J. (2017). Do minor sudden stratospheric warmings in the Southern Hemisphere (SH) impact coupling between stratosphere and mesosphere–lower thermosphere

(MLT) like major warmings? *Earth, Planets and Space*, *69*(1), 119. doi: 10.1186/s40623-017-0704-5

Fejer, B. G., Olson, M. E., Chau, J. L., Stolle, C., Lühr, H., Goncharenko, L. P., ... Nagatsuma, T. (2010). Lunar-dependent equatorial ionospheric electrodynamic effects during sudden stratospheric warmings. *Journal of Geophysical Research: Space Physics*, *115*(A8). (A00G03) doi: 10.1029/2010JA015273

Forbes, J. M. (1982). Atmospheric tides: 1. model description and results for the solar diurnal component. *Journal of Geophysical Research: Space Physics*, *87*(A7), 5222-5240. doi: 10.1029/JA087iA07p05222

Forbes, J. M., & Garrett, H. B. (1978). Thermal excitation of atmospheric tides due to insolation absorption by O3 and H2O. *Geophysical Research Letters*, *5*(12), 1013-1016. doi: 10.1029/GL005i012p01013

Forbes, J. M., & Wu, D. (2006). Solar tides as revealed by measurements of mesosphere temperature by the MLS experiment on UARS. *Journal of the Atmospheric Sciences*, *63*(7), 1776-1797. doi: 10.1175/JAS3724.1

Forbes, J. M., & Zhang, X. (2012). Lunar tide amplification during the January 2009 stratosphere warming event: Observations and theory. *Journal of Geophysical Research: Space Physics (1978–2012)*, *117*(A12). doi: 10.1029/2012JA017963

Forbes, J. M., Zhang, X., Bruinsma, S., & Oberheide, J. (2013). Lunar semidiurnal tide in the thermosphere under solar minimum conditions. *Journal of Geophysical Research: Space Physics*, *118*(4), 1788–1801.

Fritz, S., & Soules, S. (1970). Large-scale temperature changes in the stratosphere observed from Nimbus III. *Journal of the Atmospheric Sciences*, *27*(7), 1091–1097.

Funke, B., López-Puertas, M., Bermejo-Pantaleón, D., García-Comas, M., Stiller, G. P., von Clarmann, T., ... Linden, A. (2010). Evidence for dynamical coupling from the lower atmosphere to the thermosphere during a major stratospheric warming. *Geophysical Research Letters*, *37*(13). (L13803) doi: 10.1029/2010GL043619

Garcia, R. R. (1987). On the mean meridional circulation of the middle atmosphere. *Journal of the atmospheric sciences*, *44*(24), 3599–3609.

Gelaro, R., McCarty, W., Suárez, M. J., Todling, R., Molod, A., Takacs, L., ...

776 Zhao, B. (2017, 06). The Modern-Era Retrospective Analysis for Research and
777 Applications, Version 2 (MERRA-2). *Journal of Climate*, *30*(14), 5419-5454.
778 doi: 10.1175/JCLI-D-16-0758.1

779 Goncharenko, L., Chau, J. L., Condor, P., Coster, A., & Benkevitch, L. (2013).
780 Ionospheric effects of sudden stratospheric warming during moderate-to-high
781 solar activity: Case study of January 2013. *Geophysical Research Letters*,
782 *40*(19), 4982–4986. doi: 10.1002/grl.50980

783 Goncharenko, L. P., Foster, J. C., Coster, A. J., Huang, C., Aponte, N., & Paxton,
784 L. J. (2007). Observations of a positive storm phase on September 10, 2005.
785 *Journal of Atmospheric and Solar-Terrestrial Physics*, *69*(10), 1253 - 1272.
786 doi: https://doi.org/10.1016/j.jastp.2006.09.011

787 Goncharenko, L. P., Coster, A. J., Chau, J. L., & Valladares, C. E. (2010). Impact
788 of sudden stratospheric warmings on equatorial ionization anomaly. *Journal of*
789 *Geophysical Research: Space Physics*, *115*(A10). (A00G07) doi: 10.1029/
790 2010JA015400

791 Goncharenko, L. P., Coster, A. J., Plumb, R. A., & Domeisen, D. I. V. (2012). The
792 potential role of stratospheric ozone in the stratosphere-ionosphere coupling
793 during stratospheric warmings. *Geophysical Research Letters*, *39*(8). doi:
794 10.1029/2012GL051261

795 Goncharenko, L. P., & Zhang, S.-R. (2008). Ionospheric signatures of sudden strato-
796 spheric warming: Ion temperature at middle latitude. *Geophysical Research*
797 *Letters*, *35*(21). (L21103) doi: 10.1029/2008GL035684

798 Hagan, M. E., Burrage, M. D., Forbes, J. M., Hackney, J., Randel, W. J., & Zhang,
799 X. (1999). GSWM-98: Results for migrating solar tides. *Journal of Geophysical*
800 *Research: Space Physics*, *104*(A4), 6813-6827. doi: 10.1029/1998JA900125

801 Haynes, P. H., McIntyre, M. E., Shepherd, T. G., Marks, C. J., & Shine, K. P.
802 (1991). On the "downward control" of extratropical diabatic circulations by
803 eddy-induced mean zonal forces. *Journal of the Atmospheric Sciences*, *48*(4),
804 651-678. doi: 10.1175/1520-0469(1991)048⟨0651:OTCOED⟩2.0.CO;2

805 He, M., Chau, J. L., Stober, G., Hall, C. M., Tsutsumi, M., & Hoffmann, P. (2017).
806 Application of Manley-Rowe relation in analyzing nonlinear interactions be-
807 tween planetary waves and the solar semidiurnal tide during 2009 sudden
808 stratospheric warming event. *Journal of Geophysical Research: Space Physics*,

809 *122*(10), 10,783-10,795. doi: 10.1002/2017JA024630

810 Heelis, R. A., Lowell, J. K., & Spiro, R. W. (1982). A model of the high-latitude
811 ionospheric convection pattern. *Journal of Geophysical Research: Space*
812 *Physics*, *87*(A8), 6339-6345. doi: 10.1029/JA087iA08p06339

813 Hibbins, R. E., Espy, P. J., Orsolini, Y. J., Limpasuvan, V., & Barnes, R. J. (2019).
814 SuperDARN observations of semidiurnal tidal variability in the MLT and the
815 response to sudden stratospheric warming events. *Journal of Geophysical*
816 *Research: Atmospheres*, *124*(9), 4862-4872. doi: 10.1029/2018JD030157

817 Hurrell, J. W., Holland, M. M., Gent, P. R., Ghan, S., Kay, J. E., Kushner, P. J.,
818 ... Marshall, S. (2013). The community earth system model: A framework for
819 collaborative research. *Bulletin of the American Meteorological Society*, *94*(9),
820 1339-1360. doi: 10.1175/BAMS-D-12-00121.1

821 Jin, H., Miyoshi, Y., Pancheva, D., Mukhtarov, P., Fujiwara, H., & Shinagawa, H.
822 (2012). Response of migrating tides to the stratospheric sudden warming
823 in 2009 and their effects on the ionosphere studied by a whole atmosphere-
824 ionosphere model GAIA with COSMIC and TIMED/SABER observa-
825 tions. *Journal of Geophysical Research: Space Physics*, *117*(A10). doi:
826 10.1029/2012JA017650

827 Jones, K., & Rishbeth, H. (1971). The origin of storm increases of mid-latitude F-
828 layer electron concentration. *Journal of Atmospheric and Terrestrial Physics*,
829 *33*(3), 391 - 401. doi: 10.1016/0021-9169(71)90144-9

830 Karlsson, B., McLandress, C., & Shepherd, T. G. (2009). Inter-hemispheric meso-
831 spheric coupling in a comprehensive middle atmosphere model. *Journal of At-*
832 *mospheric and Solar-Terrestrial Physics*, *71*(3-4), 518–530. doi: 10.1016/j.jastp
833 .2008.08.006

834 Korenkov, Y. N., Klimenko, V. V., Klimenko, M. V., Bessarab, F. S., Korenkova,
835 N. A., Ratovsky, K. G., ... Condor, P. (2012). The global thermospheric
836 and ionospheric response to the 2008 minor sudden stratospheric warm-
837 ing event. *Journal of Geophysical Research: Space Physics*, *117*(A10). doi:
838 10.1029/2012JA018018

839 Körnich, H., & Becker, E. (2010). A simple model for the interhemispheric coupling
840 of the middle atmosphere circulation. *Advances in Space Research*, *45*(5), 661–
841 668.

Kunz, A., Pan, L. L., Konopka, P., Kinnison, D. E., & Tilmes, S. (2011). Chemical and dynamical discontinuity at the extratropical tropopause based on START08 and WACCM analyses. *Journal of Geophysical Research: Atmospheres*, *116*(D24). doi: 10.1029/2011JD016686

Labitzke, K. (1972). Temperature changes in the mesosphere and stratosphere connected with circulation changes in winter. *Journal of the Atmospheric Sciences*, *29*(4), 756–766.

Labitzke, K. (1981). Stratospheric-mesospheric midwinter disturbances: A summary of observed characteristics. *Journal of Geophysical Research: Oceans*, *86*(C10), 9665-9678. doi: 10.1029/JC086iC10p09665

Lin, C., Lin, J., Chang, L., Chen, W., Chen, C., & Liu, J. (2013). Stratospheric sudden warming effects on the ionospheric migrating tides during 2008–2010 observed by FORMOSAT-3/COSMIC. *Journal of Atmospheric and Solar-Terrestrial Physics*, *103*, 66–75.

Lindzen, R. S., & Chapman, S. (1969). Atmospheric tides. *Space science reviews*, *10*(1), 3–188.

Liu, G., Huang, W., Shen, H., Aa, E., Li, M., Liu, S., & Luo, B. (2019). Ionospheric response to the 2018 sudden stratospheric warming event at middle- and low-latitude stations over China sector. *Space Weather*, *17*(8), 1230-1240. doi: 10.1029/2019SW002160

Liu, H.-L., Bardeen, C. G., Foster, B. T., Lauritzen, P., Liu, J., Lu, G., ... others (2018). Development and validation of the whole atmosphere community climate model with thermosphere and ionosphere extension (WACCM-X 2.0). *Journal of Advances in Modeling Earth Systems*, *10*(2), 381–402.

Liu, H.-L., & Roble, R. G. (2002). A study of a self-generated stratospheric sudden warming and its mesospheric-lower thermospheric impacts using the coupled TIME-GCM/CCM3. *Journal of Geophysical Research: Atmospheres*, *107*(D23), ACL 15-1–ACL 15-18. (4695) doi: 10.1029/2001JD001533

Liu, H.-L., Wang, W., Richmond, A. D., & Roble, R. G. (2010). Ionospheric variability due to planetary waves and tides for solar minimum conditions. *Journal of Geophysical Research: Space Physics*, *115*(A6). doi: 10.1029/2009JA015188

Liu, J., Zhang, D.-H., Hao, Y.-Q., & Xiao, Z. (2019). The Comparison of Lunar

Tidal Characteristics in the Low-Latitudinal Ionosphere Between East Asian and American Sectors During Stratospheric Sudden Warming Events: 2009-2018. *Journal of Geophysical Research: Space Physics*, *124*(8), 7013-7033. doi: 10.1029/2019JA026722

Manney, G. L., Krüger, K., Pawson, S., Minschwaner, K., Schwartz, M. J., Daffer, W. H., ... Waters, J. W. (2008). The evolution of the stratopause during the 2006 major warming: Satellite data and assimilated meteorological analyses. *Journal of Geophysical Research: Atmospheres*, *113*(D11). doi: 10.1029/2007JD009097

Manney, G. L., Schwartz, M. J., Krüger, K., Santee, M. L., Pawson, S., Lee, J. N., ... Livesey, N. J. (2009). Aura microwave limb sounder observations of dynamics and transport during the record-breaking 2009 arctic stratospheric major warming. *Geophysical Research Letters*, *36*(12). (L12815) doi: 10.1029/2009GL038586

Marsh, D. R., Mills, M. J., Kinnison, D. E., Lamarque, J.-F., Calvo, N., & Polvani, L. M. (2013). Climate change from 1850 to 2005 simulated in CESM1(WACCM). *Journal of Climate*, *26*(19), 7372-7391. doi: 10.1175/JCLI-D-12-00558.1

Matsuno, T. (1971). A dynamical model of the stratospheric sudden warming. *Journal of the Atmospheric Sciences*, *28*(8), 1479–1494.

Matsushita, S. (1959). A study of the morphology of ionospheric storms. *Journal of Geophysical Research (1896-1977)*, *64*(3), 305-321. doi: 10.1029/JZ064i003p00305

Maute, A. (2017). Thermosphere-ionosphere-electrodynamics general circulation model for the ionospheric connection explorer: TIEGCM-ICON. *Space Science Reviews*, *212*(1-2), 523–551. doi: https://doi.org/10.1007/s11214-017-0330-3

McIntyre, M. E., & Palmer, T. N. (1983, 10 13). Breaking planetary waves in the stratosphere. *Nature*, *305*, 593–600. doi: 10.1038/305593a0

Neale, R. B., Richter, J., Park, S., Lauritzen, P. H., Vavrus, S. J., Rasch, P. J., & Zhang, M. (2013). The Mean Climate of the Community Atmosphere Model (CAM4) in Forced SST and Fully Coupled Experiments. *Journal of Climate*, *26*(14), 5150-5168. doi: 10.1175/JCLI-D-12-00236.1

Oyama, K.-I., Jhou, J. T., Lin, J. T., Lin, C., Liu, H., & Yumoto, K. (2014). Iono-

spheric response to 2009 sudden stratospheric warming in the Northern Hemisphere. *Journal of Geophysical Research: Space Physics*, *119*(12), 10,260-10,275. doi: 10.1002/2014JA020014

Patra, A. K., Pavan Chaitanya, P., Sripathi, S., & Alex, S. (2014). Ionospheric variability over Indian low latitude linked with the 2009 sudden stratospheric warming. *Journal of Geophysical Research: Space Physics*, *119*(5), 4044-4061. doi: 10.1002/2014JA019847

Pedatella, N. M. (2016). Impact of the lower atmosphere on the ionosphere response to a geomagnetic superstorm. *Geophysical Research Letters*, *43*(18), 9383-9389. doi: 10.1002/2016GL070592

Pedatella, N. M., Chau, J., Schmidt, H., Goncharenko, L., Stolle, C., Hocke, K., ... Siddiqui, T. (2018). How sudden stratospheric warming affects the whole atmosphere. *Eos*. doi: 10.1029/2018EO092441

Pedatella, N. M., & Forbes, J. M. (2010). Evidence for stratosphere sudden warming-ionosphere coupling due to vertically propagating tides. *Geophysical Research Letters*, *37*(11). doi: 10.1029/2010GL043560

Pedatella, N. M., Fuller-Rowell, T., Wang, H., Jin, H., Miyoshi, Y., Fujiwara, H., ... Goncharenko, L. (2014). The neutral dynamics during the 2009 sudden stratosphere warming simulated by different whole atmosphere models. *Journal of Geophysical Research: Space Physics*, *119*(2), 1306–1324. doi: 10.1002/2013JA019421

Pedatella, N. M., & Liu, H. (2013). The influence of atmospheric tide and planetary wave variability during sudden stratosphere warmings on the low latitude ionosphere. *Journal of Geophysical Research: Space Physics*, *118*(8), 5333–5347. doi: 10.1002/jgra.50492

Pedatella, N. M., Liu, H.-L., & Richmond, A. D. (2012). Atmospheric semidiurnal lunar tide climatology simulated by the whole atmosphere community climate model. *Journal of Geophysical Research: Space Physics*, *117*(A6). doi: 10.1029/2012JA017792

Pedatella, N. M., Liu, H.-L., Richmond, A. D., Maute, A., & Fang, T.-W. (2012). Simulations of solar and lunar tidal variability in the mesosphere and lower thermosphere during sudden stratosphere warmings and their influence on the low-latitude ionosphere. *Journal of Geophysical Research: Space Physics*,

941 *117*(A8). (A08326) doi: 10.1029/2012JA017858

942 Pedatella, N. M., & Maute, A. (2015). Impact of the semidiurnal lunar tide on the
943 midlatitude thermospheric wind and ionosphere during sudden stratosphere
944 warmings. *Journal of Geophysical Research: Space Physics*, *120*(12), 10,740-
945 10,753. doi: 10.1002/2015JA021986

946 Polvani, L. M., Sobel, A. H., & Waugh, D. W. (2013). *The stratosphere: dynamics,*
947 *transport, and chemistry* (Vol. 190). John Wiley & Sons.

948 Polyakova, A., Chernigovskaya, M., & Perevalova, N. (2014). Ionospheric ef-
949 fects of sudden stratospheric warmings in eastern Siberia region. *Jour-*
950 *nal of Atmospheric and Solar-Terrestrial Physics*, *120*, 15 - 23. doi:
951 https://doi.org/10.1016/j.jastp.2014.08.011

952 Prölss, G. W. (1995). Ionospheric F-region storms. *Handbook of atmospheric electro-*
953 *dynamics*, *2*, 195–248.

954 Rao, J., Garfinkel, C. I., Chen, H., & White, I. P. (2019). The 2019 New Year
955 Stratospheric Sudden Warming and Its Real-Time Predictions in Multiple S2S
956 Models. *Journal of Geophysical Research: Atmospheres*, *124*(21), 11155-11174.
957 doi: 10.1029/2019JD030826

958 Richards, P. G., Fennelly, J. A., & Torr, D. G. (1994). EUVAC: A solar EUV Flux
959 Model for aeronomic calculations. *Journal of Geophysical Research: Space*
960 *Physics*, *99*(A5), 8981-8992. doi: 10.1029/94JA00518

961 Rideout, W., & Coster, A. (2006). Automated GPS processing for global total elec-
962 tron content data. *GPS solutions*, *10*(3), 219–228. doi: 10.1007/s10291-006
963 -0029-5

964 Roble, R. G., & Ridley, E. C. (1987). An auroral model for the NCAR thermo-
965 spheric general circulation model (TGCM). *Annales Geophysicae*, *5*, 369-382.

966 Sastri, J. H. (1988). Equatorial electric fields of ionospheric disturbance dynamo ori-
967 gin. *AnGeo*, *6*, 635–642.

968 Scherhag, R. (1952). Die explosionsartigen stratosphärenerwärmungen des
969 spätwinters 1951/52. *Berichte des deutschen Wetterdienstes in der US-Zone*,
970 *6*(38), 51–63.

971 Siddiqui, T. A., Maute, A., Pedatella, N., Yamazaki, Y., Lühr, H., & Stolle, C.
972 (2018). On the variability of the semidiurnal solar and lunar tides of the equa-
973 torial electrojet during sudden stratospheric warmings. *Annales Geophysicae*,

974 *36*(6), 1545–1562. doi: 10.5194/angeo-36-1545-2018

975 Siddiqui, T. A., Maute, A., & Pedatella, N. M. (2019). On the importance of inter-
976 active ozone chemistry in Earth-System models for studying mesophere-lower
977 thermosphere tidal changes during sudden stratospheric warmings. *Jour-*
978 *nal of Geophysical Research: Space Physics*, *124*(12), 10690-10707. doi:
979 10.1029/2019JA027193

980 Siddiqui, T. A., Stolle, C., Lühr, H., & Matzka, J. (2015). On the relationship be-
981 tween weakening of the northern polar vortex and the lunar tidal amplification
982 in the equatorial electrojet. *Journal of Geophysical Research: Space Physics*,
983 *120*(11), 10006–10019. doi: 10.1002/2015JA021683

984 Siskind, D. E., Eckermann, S. D., Coy, L., McCormack, J. P., & Randall, C. E.
985 (2007). On recent interannual variability of the arctic winter mesosphere:
986 Implications for tracer descent. *Geophysical Research Letters*, *34*(9). doi:
987 10.1029/2007GL029293

988 Smith, A. K. (2012). Global dynamics of the MLT. *Surveys in Geophysics*, *33*(6),
989 1177–1230. doi: 10.1007/s10712-012-9196-9

990 Sumod, S., Pant, T., Jose, L., Hossain, M., & Kumar, K. (2012). Signatures of sud-
991 den stratospheric warming on the equatorial ionosphere-thermosphere system.
992 *Planetary and Space Science*, *63-64*, 49 - 55. doi: 10.1016/j.pss.2011.08.005

993 Tapping, K. (2013). The 10.7 cm solar radio flux (F10.7). *Space Weather*, *11*(7),
994 394–406.

995 van Loon, H., Jenne, R. L., & Labitzke, K. (1973). Zonal harmonic standing waves.
996 *Journal of Geophysical Research (1896-1977)*, *78*(21), 4463-4471. doi: 10.1029/
997 JC078i021p04463

998 Vieira, F., Fagundes, P. R., Venkatesh, K., Goncharenko, L. P., & Pillat, V. G.
999 (2017). Total electron content disturbances during minor sudden strato-
1000 spheric warming, over the Brazilian region: A case study during January 2012.
1001 *Journal of Geophysical Research: Space Physics*, *122*(2), 2119-2135. doi:
1002 10.1002/2016JA023650

1003 Vineeth, C., Kumar Pant, T., & Sridharan, R. (2009). Equatorial counter elec-
1004 trojets and polar stratospheric sudden warmings - a classical example of high
1005 latitude-low latitude coupling? *Annales Geophysicae*, *27*(8), 3147–3153. doi:
1006 10.5194/angeo-27-3147-2009

Waters, J. W., Froidevaux, L., Harwood, R. S., Jarnot, R. F., Pickett, H. M., Read, W. G., ... Walch, M. J. (2006). The Earth observing system microwave limb sounder (EOS MLS) on the aura satellite. *IEEE Transactions on Geoscience and Remote Sensing*, *44*(5), 1075-1092.

Waugh, D. W., & Randel, W. J. (1999). Climatology of Arctic and Antarctic Polar Vortices Using Elliptical Diagnostics. *Journal of the Atmospheric Sciences*, *56*(11), 1594-1613. doi: 10.1175/1520-0469(1999)056⟨1594:COAAAP⟩2.0.CO;2

Weimer, D. R. (2005). Improved ionospheric electrodynamic models and application to calculating joule heating rates. *Journal of Geophysical Research: Space Physics*, *110*(A5). doi: 10.1029/2004JA010884

Xiong, J., Wan, W., Ding, F., Liu, L., Ning, B., & Niu, X. (2013). Coupling between mesosphere and ionosphere over beijing through semidiurnal tides during the 2009 sudden stratospheric warming. *Journal of Geophysical Research: Space Physics*, *118*(5), 2511-2521. doi: 10.1002/jgra.50280

Yadav, S., Pant, T. K., Choudhary, R., Vineeth, C., Sunda, S., Kumar, K., ... Mukherjee, S. (2017). Impact of sudden stratospheric warming of 2009 on the equatorial and low-latitude ionosphere of the indian longitudes: A case study. *Journal of Geophysical Research: Space Physics*, *122*(10).

Yamazaki, Y., Matthias, V., Miyoshi, Y., Stolle, C., Siddiqui, T., Kervalishvili, G., ... Alken, P. (2020). September 2019 Antarctic Sudden Stratospheric Warming: Quasi-6-day wave burst and ionospheric effects. *Geophysical Research Letters*, *47*(1), e2019GL086577. doi: 10.1029/2019GL086577

Yamazaki, Y., Richmond, A., Maute, A., Liu, H.-L., Pedatella, N., & Sassi, F. (2014). On the day-to-day variation of the equatorial electrojet during quiet periods. *Journal of Geophysical Research: Space Physics*, *119*(8), 6966–6980.

Yamazaki, Y., Richmond, A., & Yumoto, K. (2012). Stratospheric warmings and the geomagnetic lunar tide: 1958–2007. *Journal of Geophysical Research: Space Physics (1978–2012)*, *117*(A4). doi: 10.1029/2012JA017514

Yiğit, E., & Medvedev, A. S. (2015). Internal wave coupling processes in Earth's atmosphere. *Advances in Space Research*, *55*(4), 983 - 1003. doi: 10.1016/j.asr.2014.11.020

Yokoyama, N., & Kamide, Y. (1997). Statistical nature of geomagnetic storms.

Journal of Geophysical Research: Space Physics, *102*(A7), 14215-14222. doi: 10.1029/97JA00903

Yue, X., Schreiner, W. S., Lei, J., Rocken, C., Hunt, D. C., Kuo, Y.-H., & Wan, W. (2010). Global ionospheric response observed by COSMIC satellites during the January 2009 stratospheric sudden warming event. *Journal of Geophysical Research: Space Physics*, *115*(A11). doi: 10.1029/2010JA015466

Zhang, X., & Forbes, J. M. (2014). Lunar tide in the thermosphere and weakening of the northern polar vortex. *Geophysical Research Letters*, *41*(23), 8201–8207. doi: 10.1002/2014GL062103

Zhang, X., Forbes, J. M., & Hagan, M. E. (2010). Longitudinal variation of tides in the MLT region: 1. Tides driven by tropospheric net radiative heating. *Journal of Geophysical Research: Space Physics*, *115*(A6). doi: 10.1029/2009JA014897

Table 1. TIE-GCM simulations: (left to right) experiment setup and the representation of geomagnetic and lower atmospheric forcings in the model runs.

Experiment setup	Geomagnetic Forcing	Lower atmospheric forcing
S1	On	On
S2	Off	On

Figure 1. Daily zonal mean temperature (K) averaged between 70° and 80°N as a function of pressure is presented from (a) Aura MLS observations (c) SD-WACCM-X simulations for the 2009 SSW. The same is presented in Figures 1b and 1d, except for the 2019 SSW. The vertical dashed black lines mark the day of PVW for the corresponding SSWs.

Figure 2. Daily zonal mean zonal wind (ZMZW) (m/s) at 60°N as a function of pressure is presented from SD-WACCM-X simulations for (a) 2009 SSW (c) 2019 SSW. The Kp index and solar flux levels are presented for the 2009 SSW in Figure 2b and for the 2019 SSW in Figure 2d. The vertical dashed black lines mark the day of PVW for the corresponding SSWs.

Figure 3. Planetary wave 1 amplitude of temperature at 10 hPa (∼30 km) from SD-WACCM-X simulations for (a) 2009 SSW (b) 2019 SSW. The same is presented for planetary wave 2 for (c) 2009 SSW and (d) 2019 SSW. The vertical white dashed lines mark the day of PVW for the corresponding SSWs.

Figure 4. SW2 tidal amplitude (a) and phase (b) in neutral temperature at 1×10^{-4} hPa (∼110 km) from SD-WACCM-X for the 2009 SSW event. The same is presented for M2 tidal amplitude (c) and phase (d). The vertical white dashed lines mark the day of PVW for the corresponding SSWs.

Figure 5. Same as Figure 4 except for the 2019 SSW event.

Figure 6. Amplitude of M2 tide at 110 km from SABER V2.0 temperature measurements for (a) 2009 SSW (b) 2019 SSW. The vertical white dashed lines mark the day of PVW for the corresponding SSWs.

Figure 7. Daily TEC perturbations (ΔTEC) over Europe from GPS TEC observations between December 26, 2018 and January 6, 2019 at 12 UT.

Figure 8. Daily averaged (a) TEC and (b) TEC perturbations (ΔTEC) over Europe from GPS TEC observations as a function of universal time for the 2019 SSW. The contour lines in (b) are only plotted when absolute ΔTEC exceeds 1 TECu. The vertical black dashed lines mark the day of PVW.

Figure 9. Same as Figure 8 except for the 2009 SSW.

Figure 10. TIE-GCM derived daily averaged TEC over Europe for simulation setup (a) S1 and (b) S2, as a function of universal time for the 2019 SSW. The difference of (a) and (b) is plotted in (c). The filled contour lines in (c) are only plotted when absolute TEC difference exceeds 1 TECu. The dashed black and blue open contour lines mark the contribution of geomagnetic forcing to the TEC variability at 40 and 80% levels, respectively. The vertical black dashed lines mark the day of PVW.

Figure 11. Same as Figure 10 except for the 2009 SSW.

Figure 1.

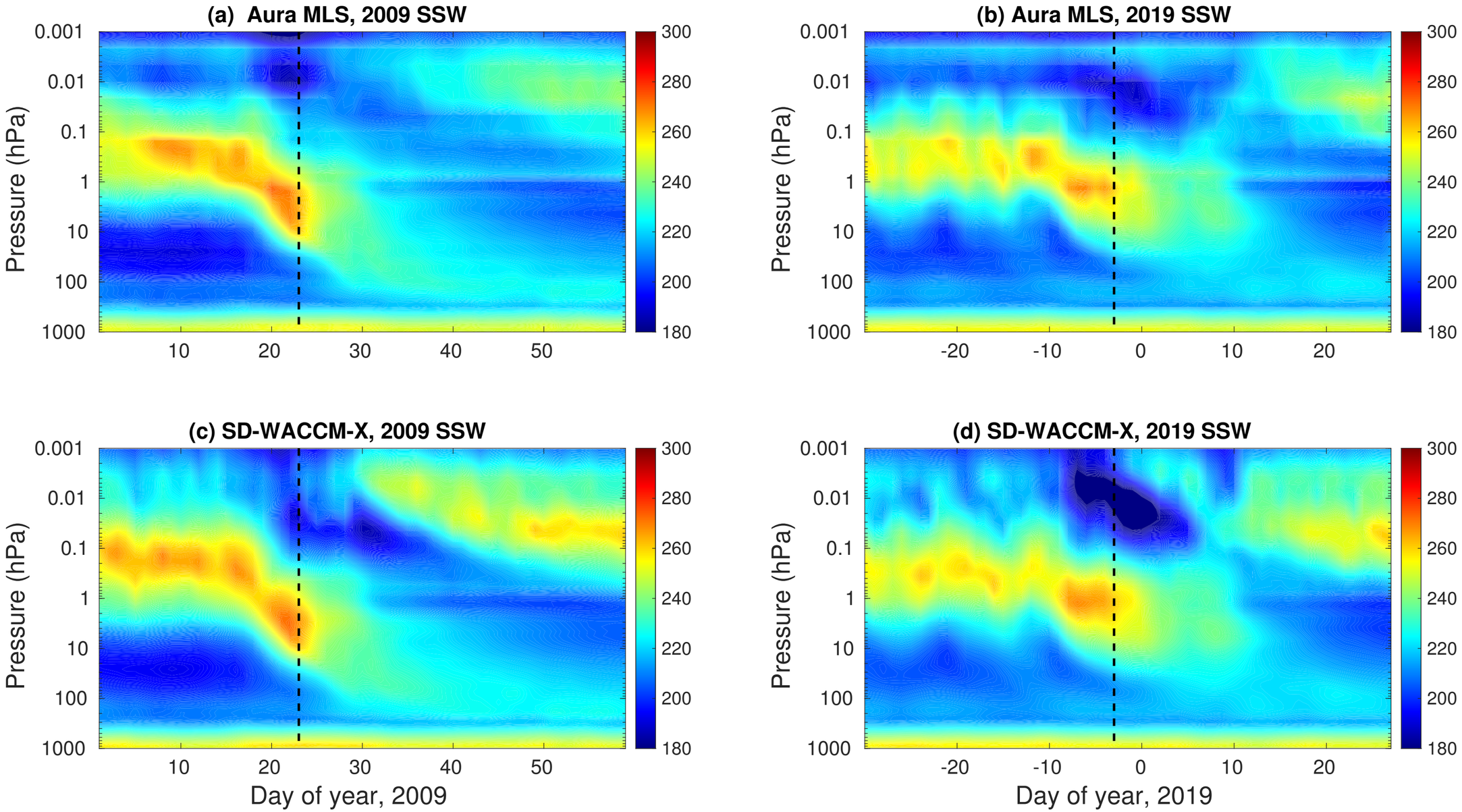
Zonal mean temperature (K), 70-80 N
(a) Aura MLS, 2009 SSW
(b) Aura MLS, 2019 SSW
(c) SD-WACCM-X, 2009 SSW
(d) SD-WACCM-X, 2019 SSW
Pressure (hPa)
0.001
0.01
0.1
1
10
100
1000
300
280
260
240
220
200
180
10
20
30
40
50
-20
-10
0
10
20
Day of year, 2009
Day of year, 2019

Figure 2.

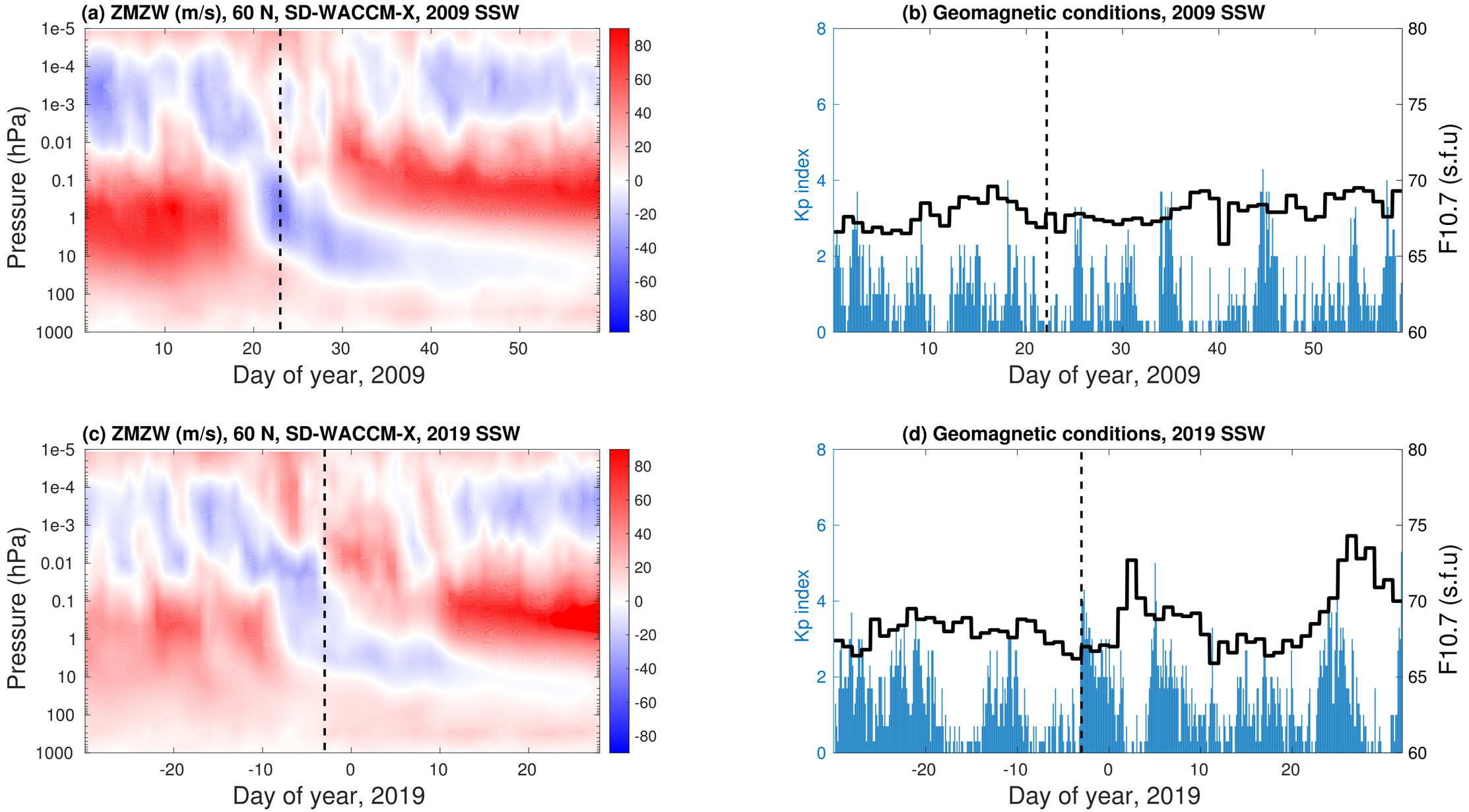
(a) ZMZW (m/s), 60 N, SD-WACCM-X, 2009 SSW
Pressure (hPa)
1e-5
1e-4
1e-3
0.01
0.1
1
10
100
1000
10
20
30
40
50
Day of year, 2009
80
60
40
20
0
-20
-40
-60
-80
(b) Geomagnetic conditions, 2009 SSW
Kp index
F10.7 (s.f.u)
0
2
4
6
8
60
65
70
75
80
10
20
30
40
50
Day of year, 2009
(c) ZMZW (m/s), 60 N, SD-WACCM-X, 2019 SSW
Pressure (hPa)
1e-5
1e-4
1e-3
0.01
0.1
1
10
100
1000
-20
-10
0
10
20
Day of year, 2019
80
60
40
20
0
-20
-40
-60
-80
(d) Geomagnetic conditions, 2019 SSW
Kp index
F10.7 (s.f.u)
0
2
4
6
8
60
65
70
75
80
-20
-10
0
10
20
Day of year, 2019

Figure 3.

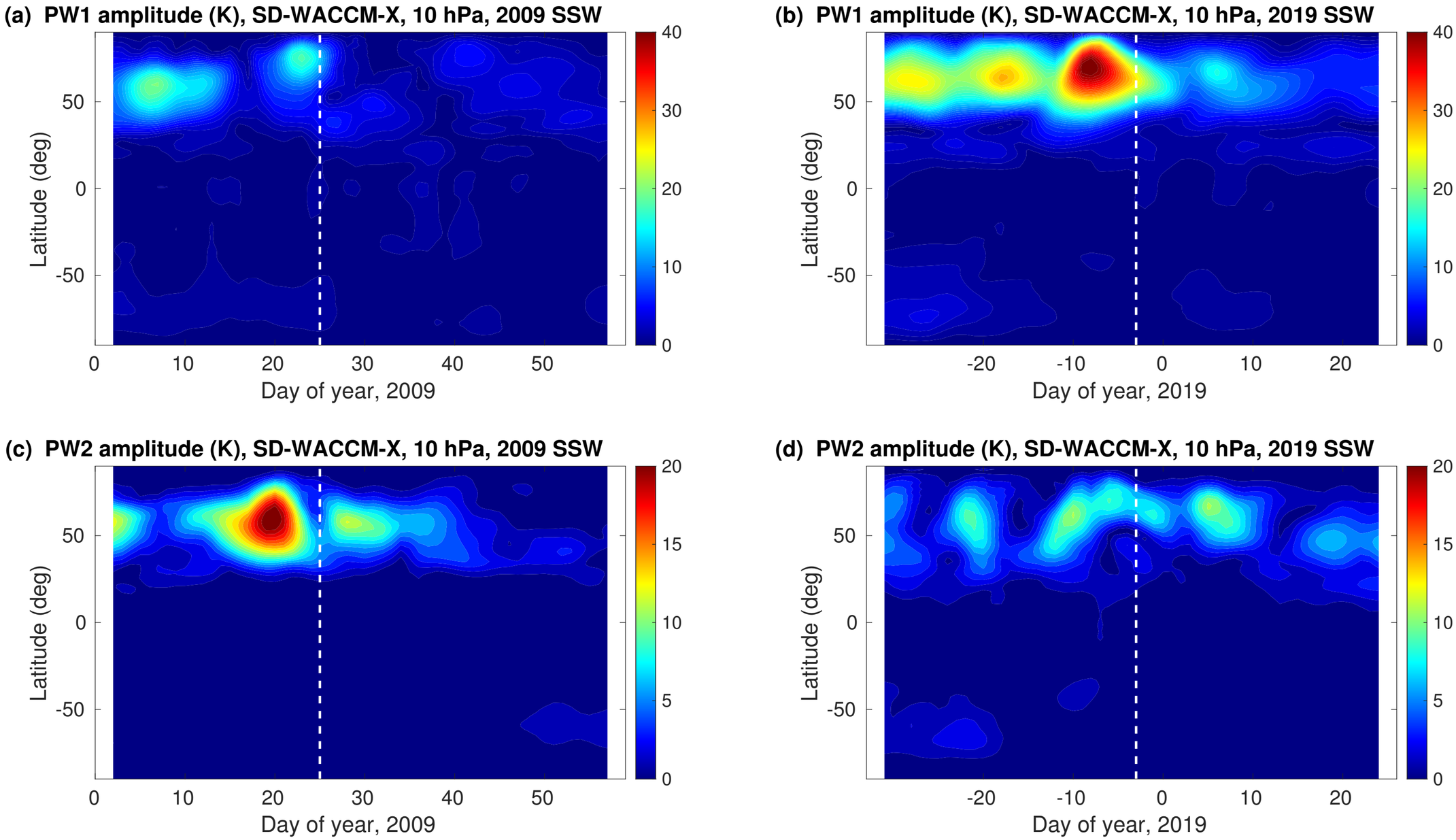
(a) PW1 amplitude (K), SD-WACCM-X, 10 hPa, 2009 SSW
Latitude (deg)
50
0
-50
0
10
20
30
40
50
Day of year, 2009
40
30
20
10
0
(b) PW1 amplitude (K), SD-WACCM-X, 10 hPa, 2019 SSW
Latitude (deg)
50
0
-50
-20
-10
0
10
20
Day of year, 2019
40
30
20
10
0
(c) PW2 amplitude (K), SD-WACCM-X, 10 hPa, 2009 SSW
Latitude (deg)
50
0
-50
0
10
20
30
40
50
Day of year, 2009
20
15
10
5
0
(d) PW2 amplitude (K), SD-WACCM-X, 10 hPa, 2019 SSW
Latitude (deg)
50
0
-50
-20
-10
0
10
20
Day of year, 2019
20
15
10
5
0

Figure 4.

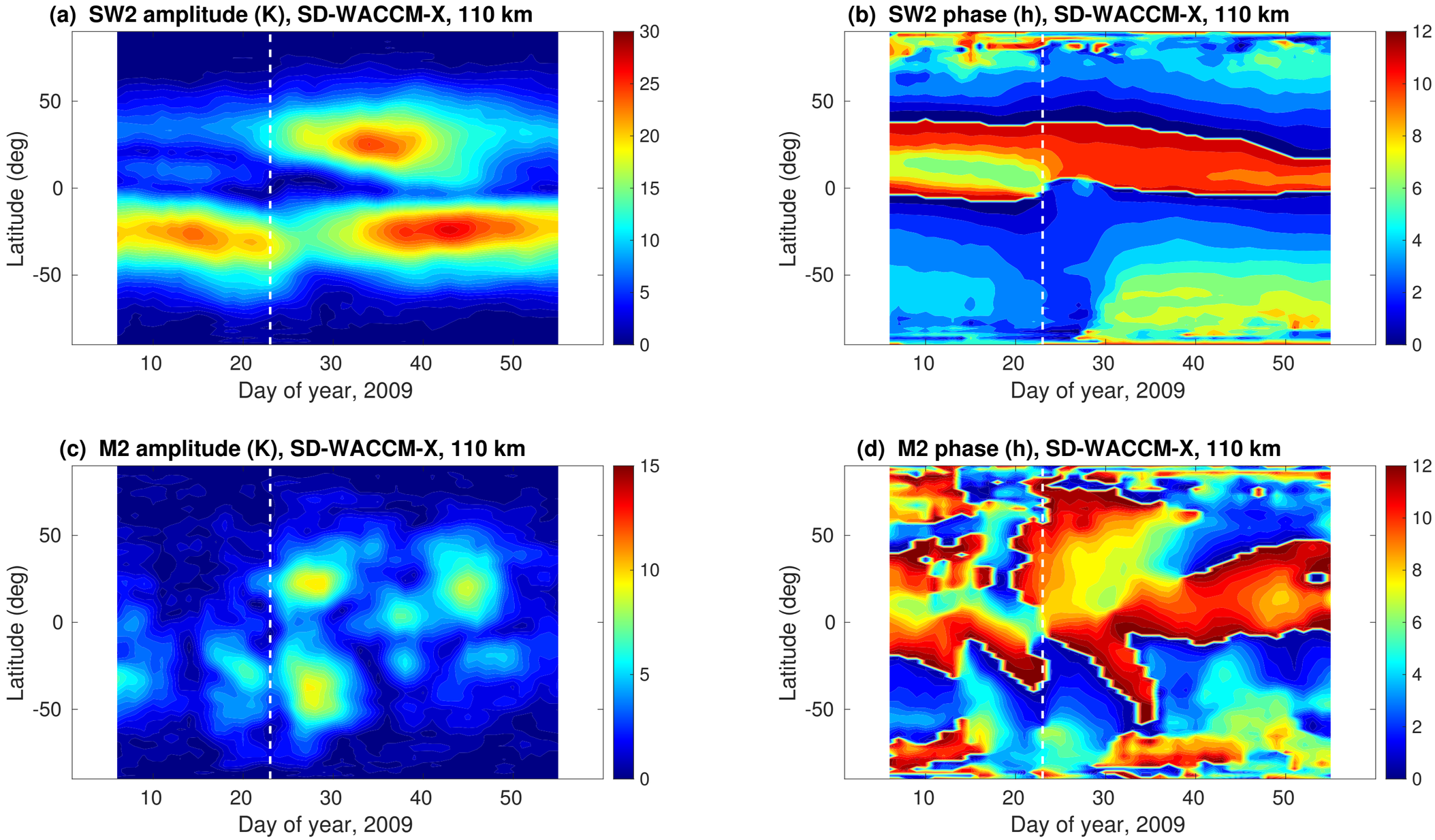
(a) SW2 amplitude (K), SD-WACCM-X, 110 km
(b) SW2 phase (h), SD-WACCM-X, 110 km
(c) M2 amplitude (K), SD-WACCM-X, 110 km
(d) M2 phase (h), SD-WACCM-X, 110 km
Latitude (deg)
Day of year, 2009
50
0
-50
10
20
30
40
50
0
5
10
15
20
25
30
2
4
6
8
12

Figure 5.

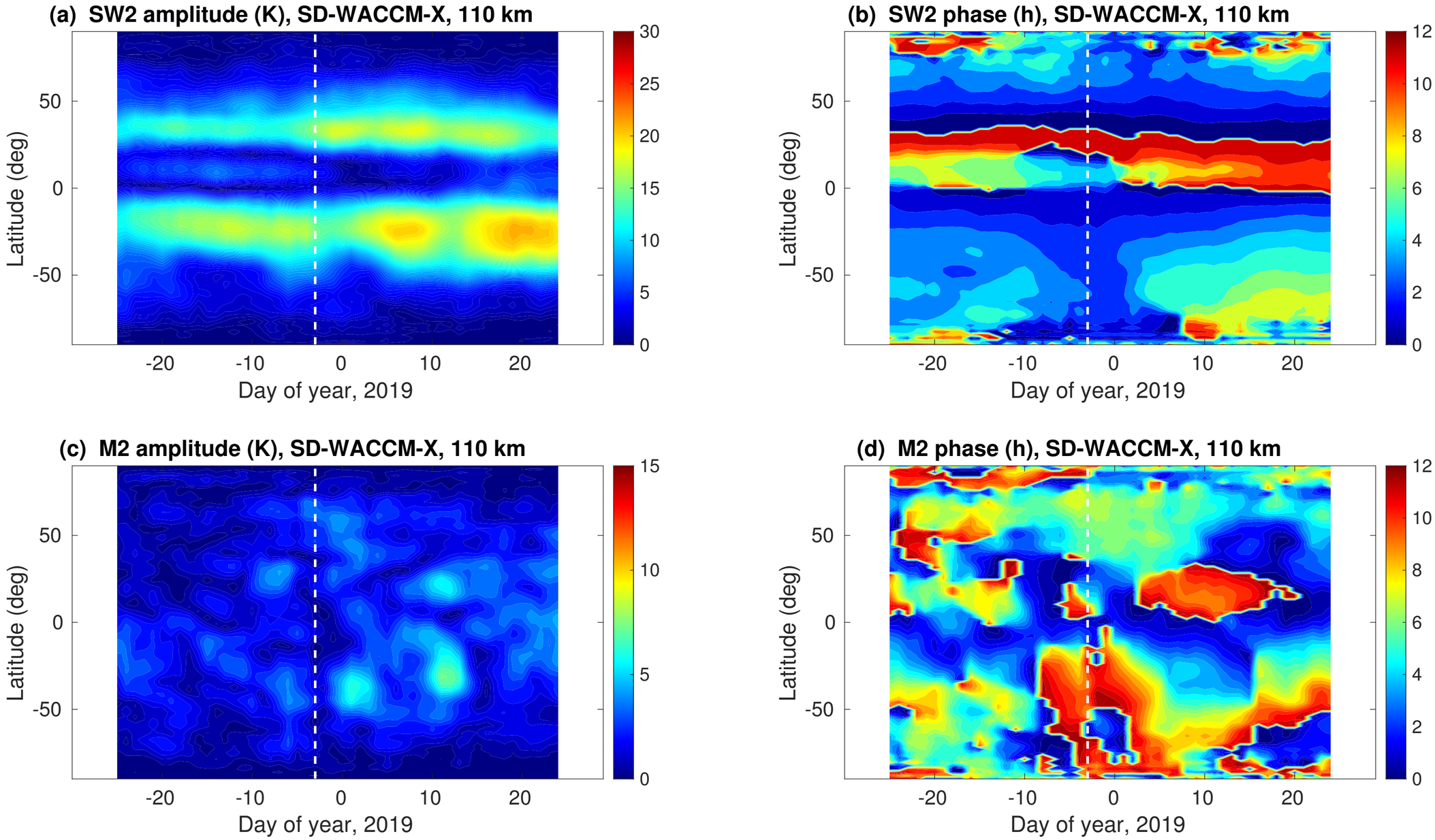
(a) SW2 amplitude (K), SD-WACCM-X, 110 km
(b) SW2 phase (h), SD-WACCM-X, 110 km
(c) M2 amplitude (K), SD-WACCM-X, 110 km
(d) M2 phase (h), SD-WACCM-X, 110 km
Latitude (deg)
Day of year, 2019
50
0
-50
-20
-10
0
10
20
30
25
20
15
10
5
0
12
10
8
6
4
2
0

Figure 6.

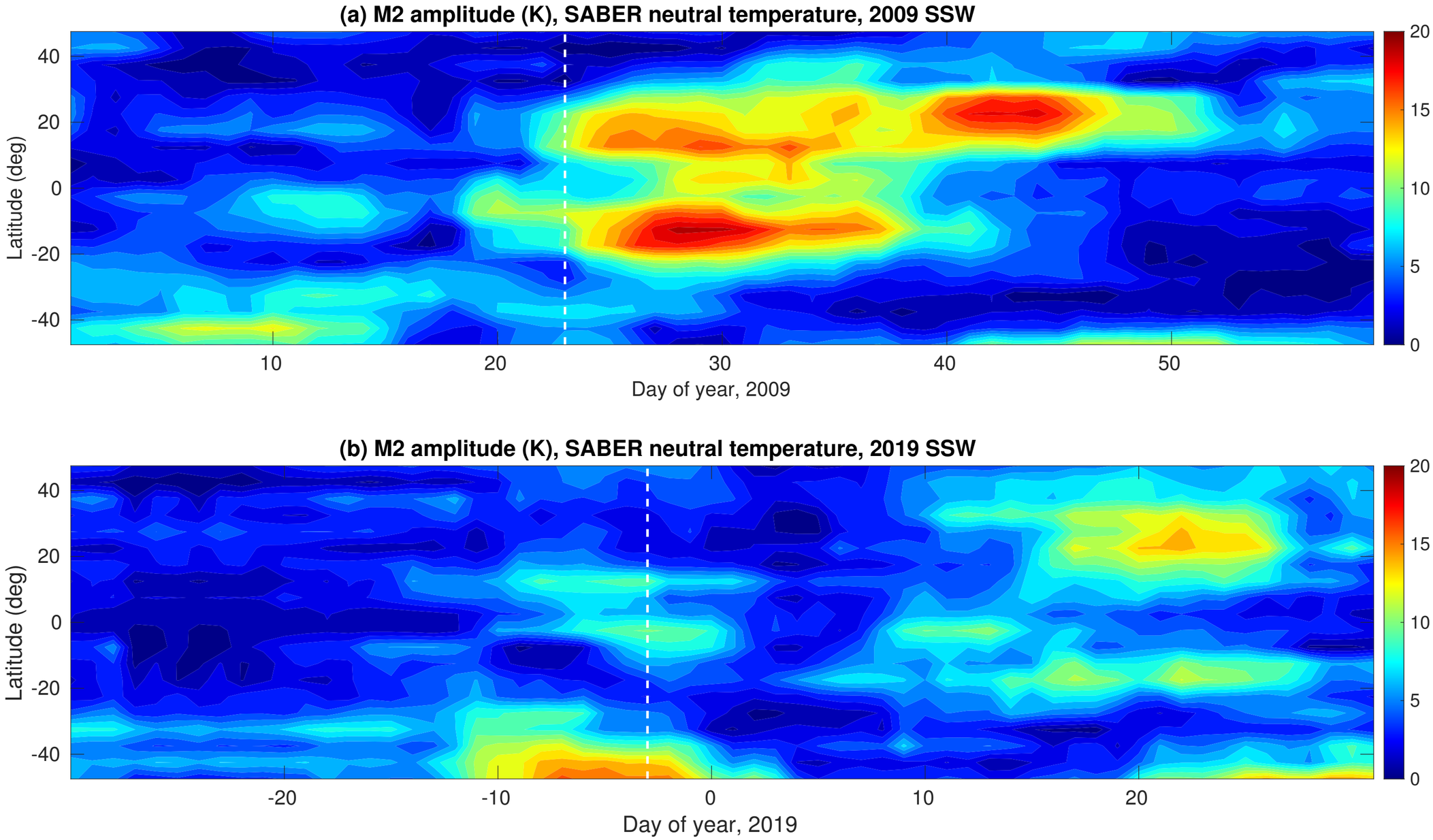
(a) M2 amplitude (K), SABER neutral temperature, 2009 SSW
Latitude (deg)
40
20
0
-20
-40
10
20
30
40
50
Day of year, 2009
20
15
10
5
0
(b) M2 amplitude (K), SABER neutral temperature, 2019 SSW
Latitude (deg)
40
20
0
-20
-40
-20
-10
0
10
20
Day of year, 2019
20
15
10
5
0

Figure 7.

ΔTEC over Europe at 12 UT

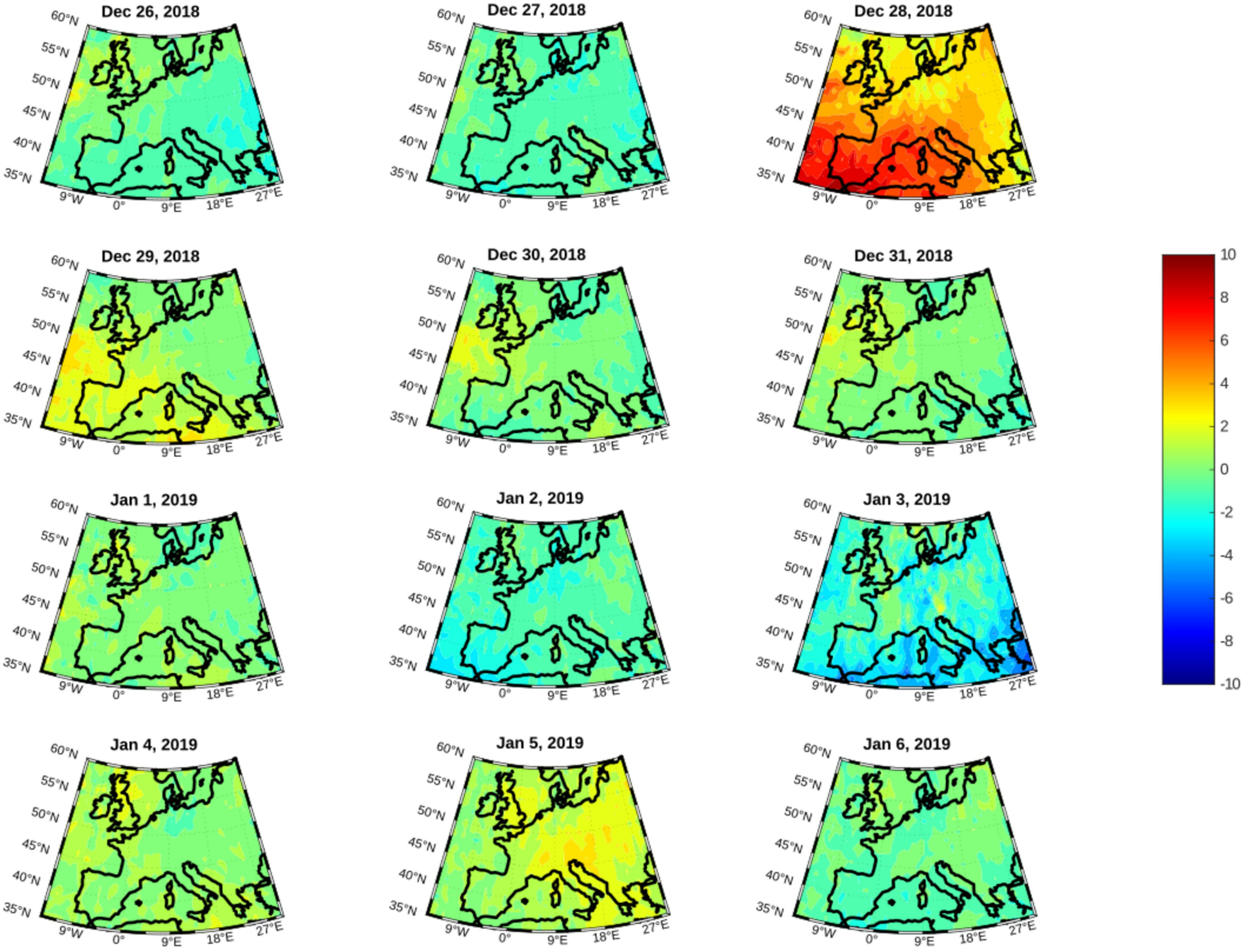

Figure 8.

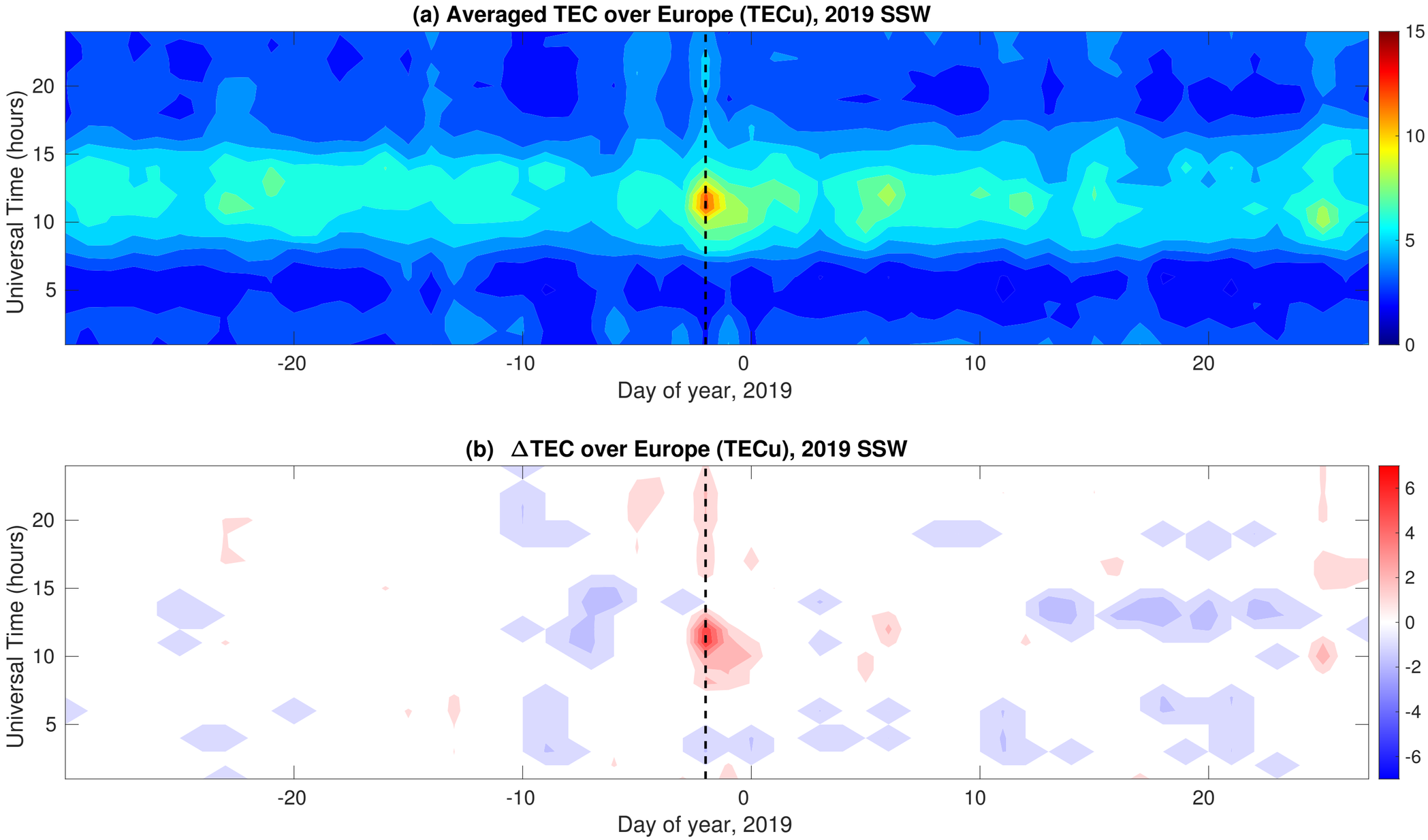
(a) Averaged TEC over Europe (TECu), 2019 SSW
Universal Time (hours)
5
10
15
20
-20
-10
0
10
20
Day of year, 2019
0
5
10
15
(b) ΔTEC over Europe (TECu), 2019 SSW
Universal Time (hours)
5
10
15
20
-20
-10
0
10
20
Day of year, 2019
-6
-4
-2
0
2
4
6

Figure 9.

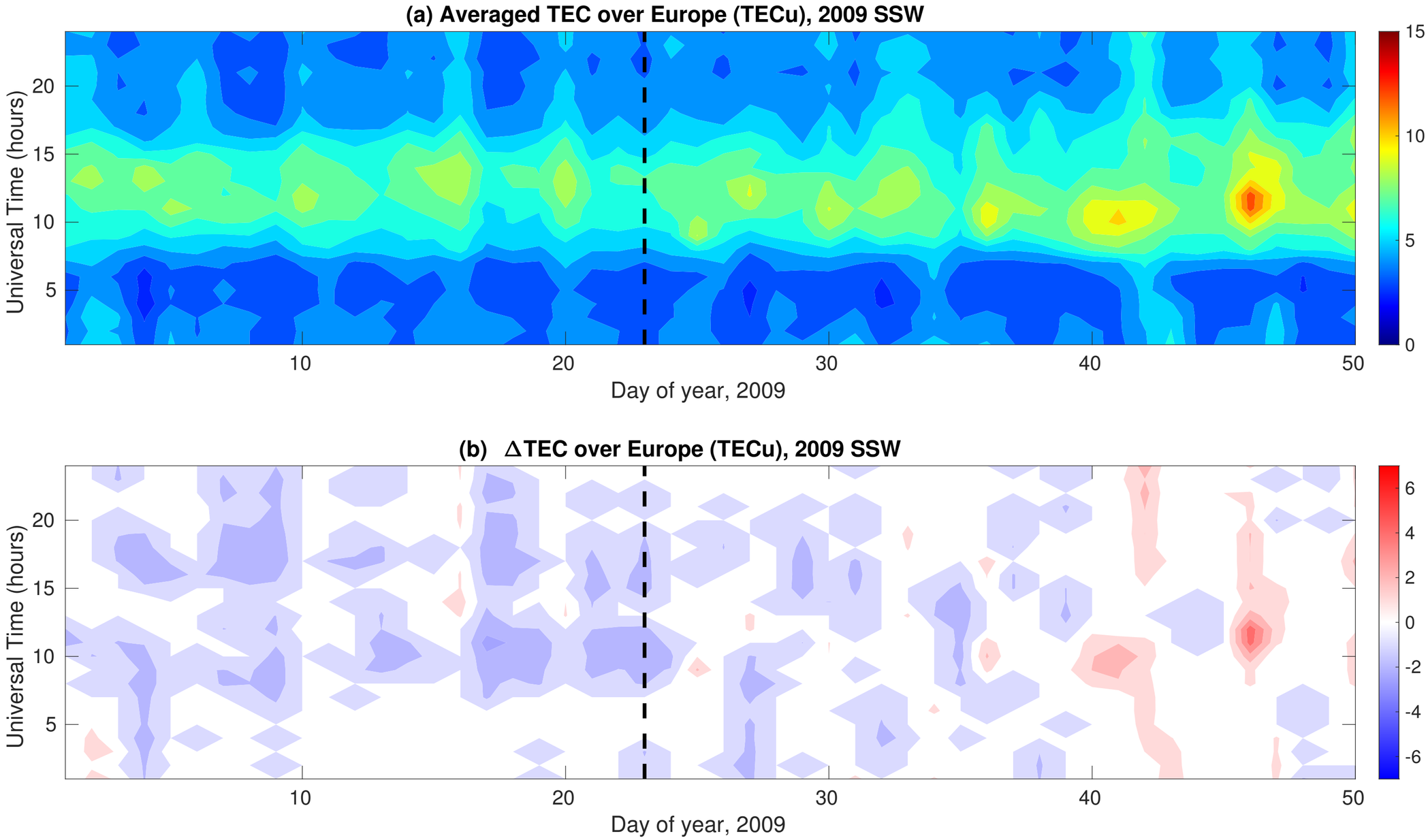
(a) Averaged TEC over Europe (TECu), 2009 SSW
Universal Time (hours)
5
10
15
20
10
20
30
40
50
Day of year, 2009
0
5
10
15
(b) ΔTEC over Europe (TECu), 2009 SSW
Universal Time (hours)
5
10
15
20
10
20
30
40
50
Day of year, 2009
-6
-4
-2
0
2
4
6

Figure 10.

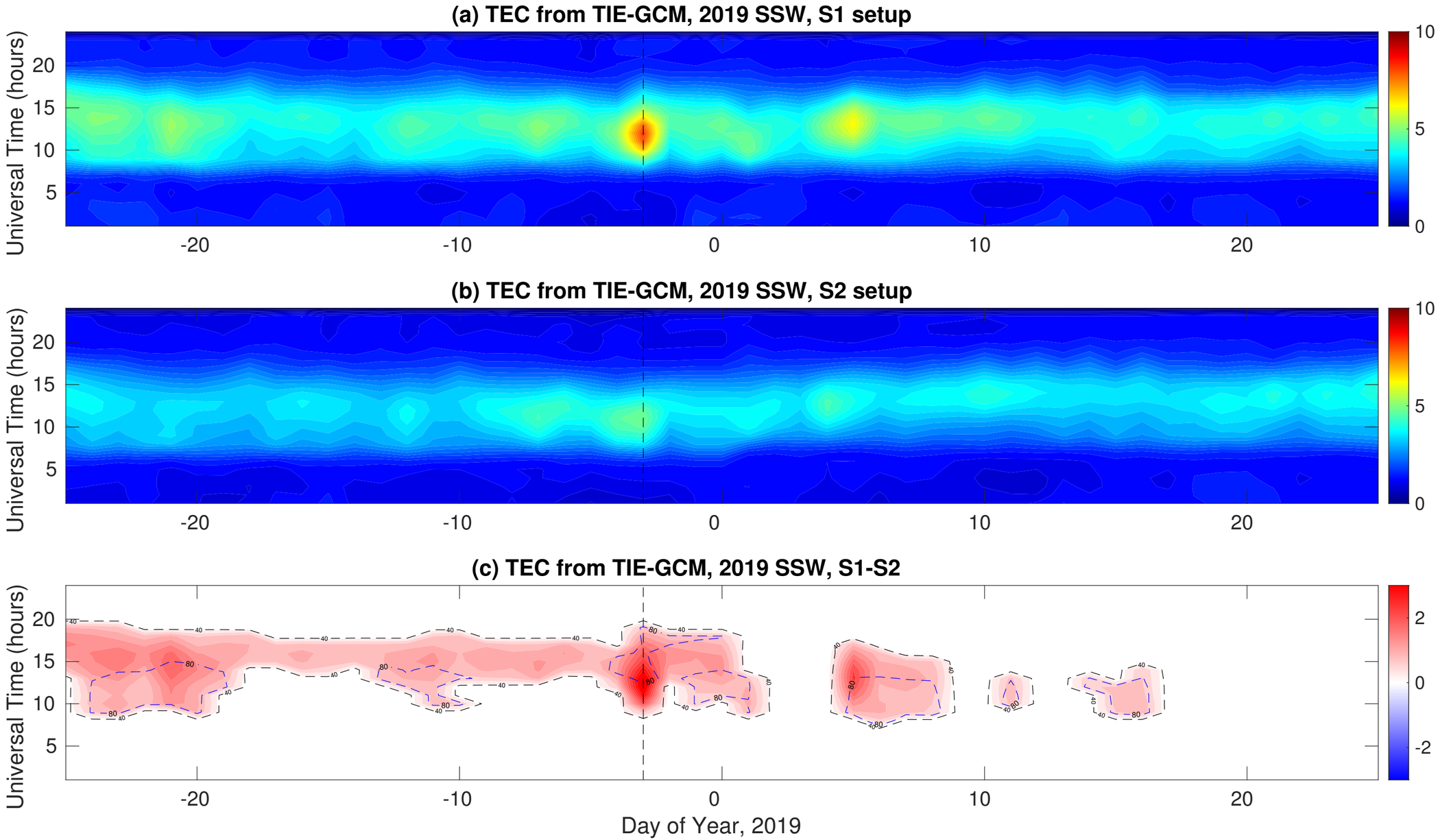
(a) TEC from TIE-GCM, 2019 SSW, S1 setup
(b) TEC from TIE-GCM, 2019 SSW, S2 setup
(c) TEC from TIE-GCM, 2019 SSW, S1-S2
Universal Time (hours)
Day of Year, 2019
5
10
15
20
-20
-10
0
10
20
40
80
-2
0
2

Figure 11.

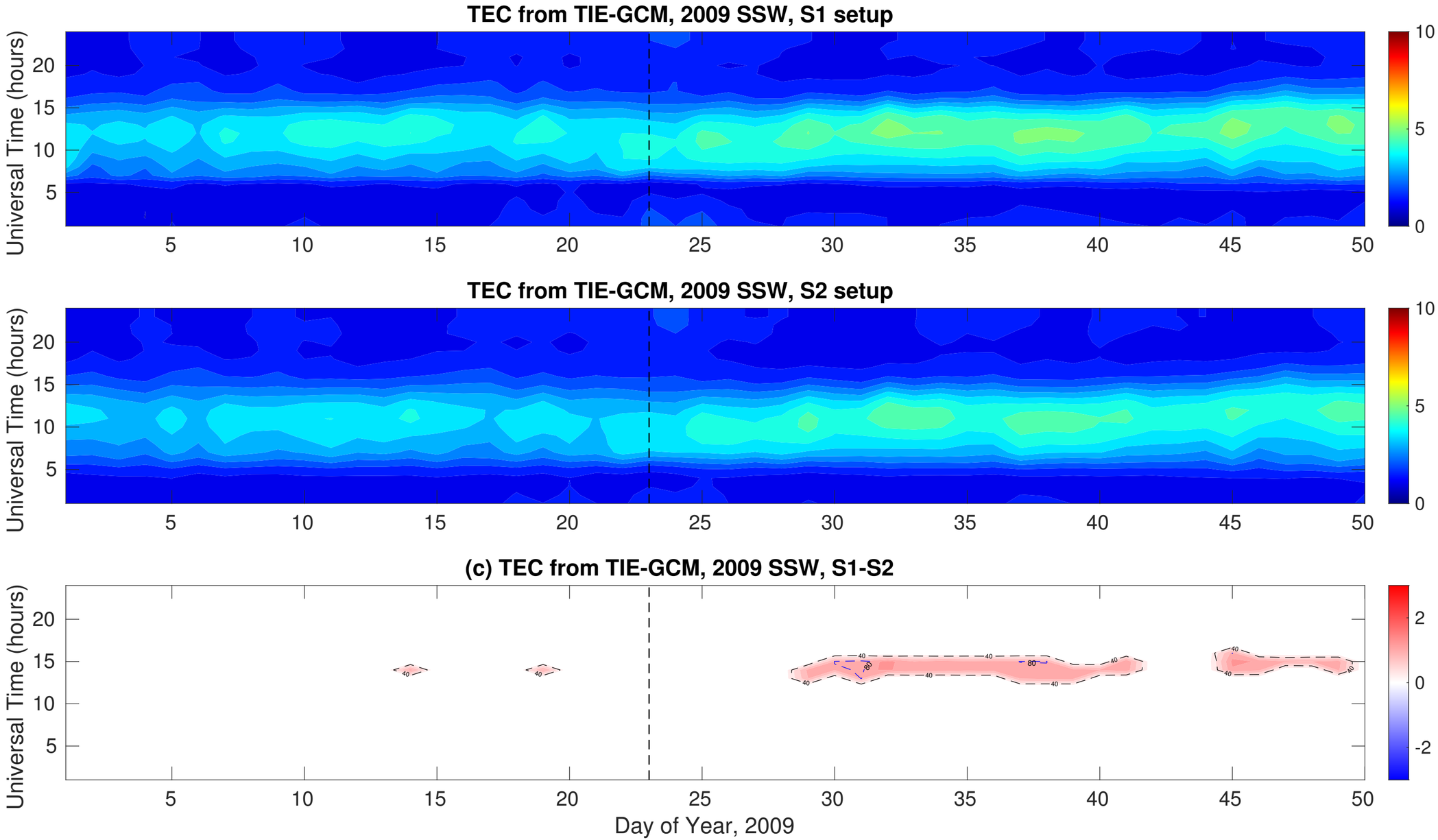
TEC from TIE-GCM, 2009 SSW, S1 setup
Universal Time (hours)
TEC from TIE-GCM, 2009 SSW, S2 setup
Universal Time (hours)
(c) TEC from TIE-GCM, 2009 SSW, S1-S2
Universal Time (hours)
Day of Year, 2009